Appendix B:
Conceptual Design of the System Telescopes

March 19, 1997

In this appendix we present design concepts for the system telescopes. These concepts build upon the knowledge developed in the design, the construction, the installation and commissioning, and the operation of the HEGRA IACT system [1, 2]. For this system, the Max-Planck-Institut für Kernphysik in Heidelberg is responsible for the high-resolution cameras, their readout electronics, most of the trigger and data acquisition system, and the complete control software including the telescope steering [3].

For a large system of IACTs such as the one discussed in this Letter of Intent, reliability and efficient production and commissioning rank higher than for previous IACTs. In the design of the mount and dish, we plan to make use of the large base of know-how available in two related areas, namely the engineering of large antenna dishes for radio astronomy and communications purposes (see e.g. [4]), and the engineering of solar concentrators (see [5, 6]). These two types of systems are, in their typical sizes and layouts, rather similar to the planned Cherenkov telescopes and bracket them, as far as performance is concerned: radio and communications dishes range from similar mechanical requirements on the stability of the dish (for cm wavelengths) to requirements which are one to almost two orders of magnitude more stringent (for the modern mm and sub-mm antennas), whereas solar concentrators provide imaging with a point spread function which is typically one order of magnitude worse than required for an IACT, although some of the latest-generation dishes come within a factor of two. In both fields, considerable emphasis has been given to the cost-effective design and production of dishes. To some extent, also multi-mirror optical telescopes provide interesting solutions; in particular the Hobby-Eberly telescope is in its primary mirror truss [7] rather similar to the structures considered for our IACTs; of course, performance requirements are significantly higher in the case of such an optical telescope.

The concepts presented in the following should be considered as a baseline, of which we are confident that it will fulfill the required tasks and that it can be built with little technical risk. In the next phase, and with the know-how brought in by potential additional collaborators, we do expect the designs to evolve further, and maybe even change significantly in some areas.

1 Overview

The proposed system telescopes use an alt-azimuth mount, a segmented mirror with a total area of 82 m^2 based on Davies-Cotton optics [8] with 12 m to 15 m focal length, and a high-resolution camera with conventional photomultiplier tubes and a pulse shape recording readout.

1.1 Mount and Mirror Dish

Various options are under study concerning the mechanics of the mount and mirror dish of the system telescopes. Fig. 1 illustrates one design study, following ideas [9] developed for a DRAO proposal concerning an array of radio telescopes. The mirrors are supported by a space frame with triangular cells. Contrary to a conventional alt-azimuth mount, the mirror dish is supported at three points arranged symmetrically; for altitude adjustment it rotates around the axis formed by two of the support points, while the third support point is moved by a linear drive. For positioning in azimuth, the whole assembly can be rotated around the azimuth axis. As discussed in more detail below, this modified mount offers certain advantages concerning the stability of the mirror dish. Another more conventional design option will be discussed in the body of this paper.

1.2 Mirror

The mirror (Fig. 2) is composed of 420 individual aluminum mirrors of 50 cm diameter. These mirrors have a focal length of 12 m to 15 m and are arranged in a Davies-Cotton [8] fashion, following a sphere with the focal

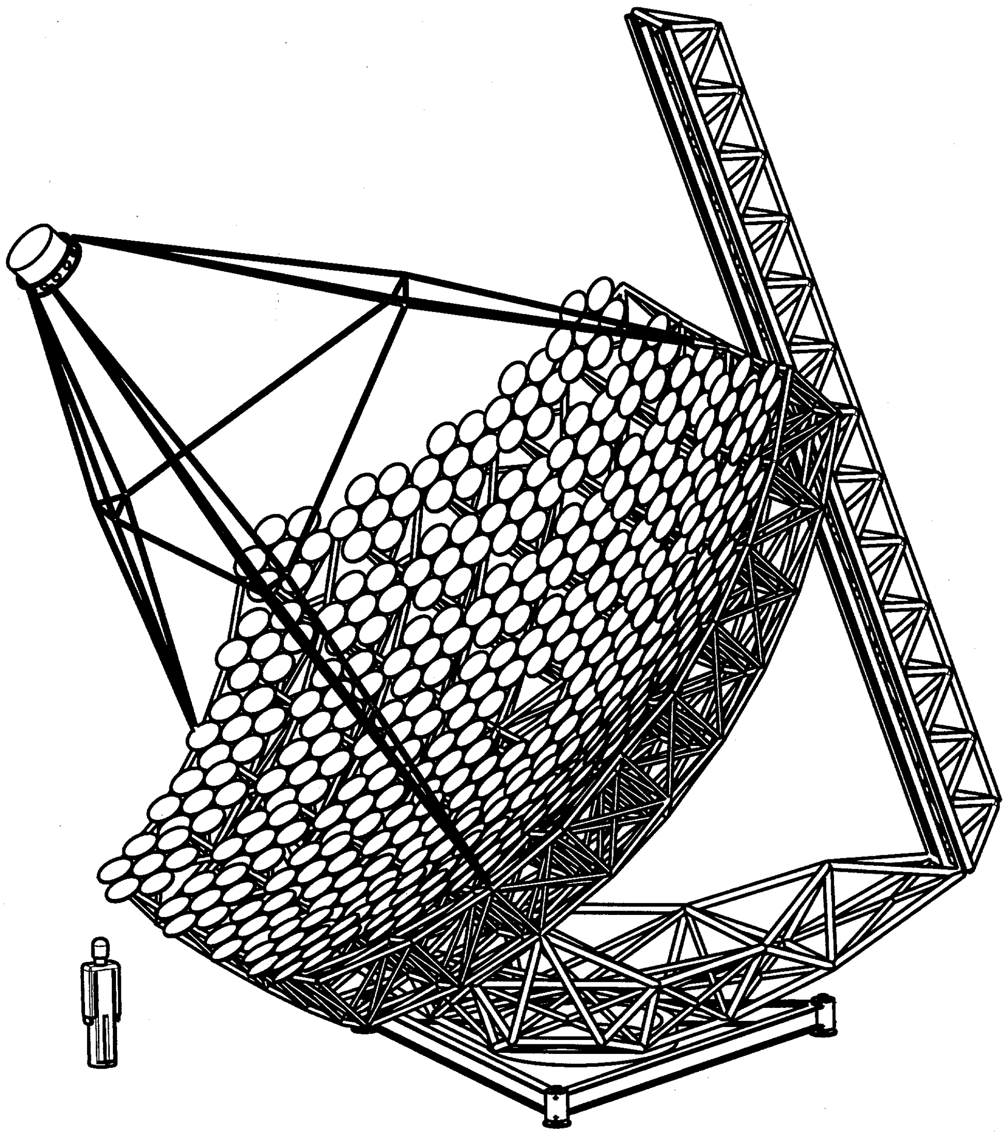

Figure 1: *Design study of an array telescope with its tiled mirror and alt-azimuth mount.*

point in its center. Compared to potentially more convenient, square-meter sized mirrors, the small mirrors are available at a drastically reduced cost per unit area. Furthermore, they offer improved imaging performance, as discussed further below. In order to limit the assembly time and the amount of on-site adjustments, groups of seven mirrors are pre-assembled into 60 mirror 'clusters'. The relative alignment of mirrors within a cluster is performed only once and then fixed, during the assembly of the cluster at a home institute or factory. Clusters as a whole can be remotely adjusted in order to provide optimal imaging properties.

1.3 Imaging Camera

At least initially, we propose to use a conventional PMT camera. The field of view of the camera should cover 4°, governed by the expected extent of potential sources. The size and number of pixels is correlated with the cost of the readout system; if a relatively inexpensive readout can be realized, the preference would be (for $f = 12$ m) to use 30 mm phototubes, resulting in a pixel size of about 0.15°, and about 800 pixels to cover the field of view. In case the presently available (HEGRA-IACT) readout has to be used, larger 52 mm, 0.25° pixels are called for; in this case, less than 300 pixels are needed. The pixel size is uniform throughout the field of view. In particular for the study of extended sources, camera homogeneity is important.

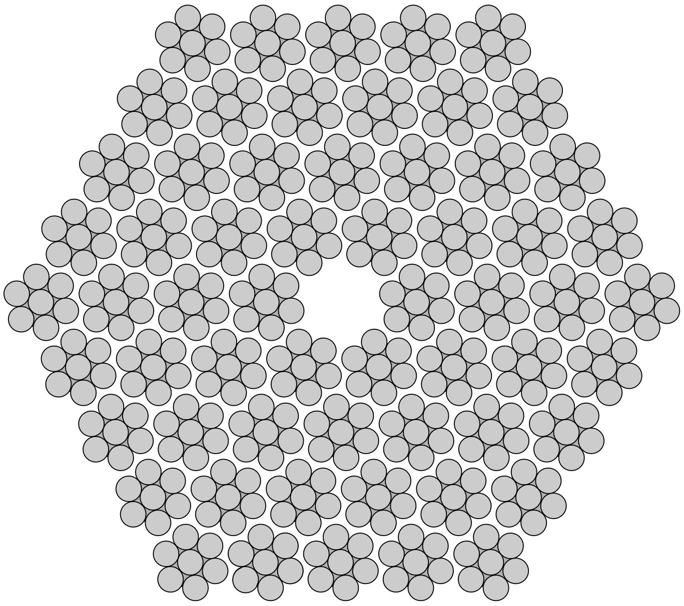

Figure 2: *The telescope mirror, consisting of 420 individual mirror tiles, grouped into 60 clusters of 7 mirrors each. To better illustrate the division into clusters, the spacing between clusters is greatly exaggerated.*

1.4 Trigger System

A telescope is triggered by a coincidence of 2 to 4 pixels of a camera (depending on the pixel size), with the additional (hardware) requirement that the trigger pixels are neighbored, to suppress noise triggers. A telescope cell (four telescopes at the corners of a square) is triggered if a minimal number of cell telescopes trigger; normally, the system will be operated with a 3-telescope or 4-telescope coincidence, but for special runs (short term observations and scans), a two-telescope trigger may be more effective. In either mode, background from local muons - a major source of triggers for large single telescopes - is strongly suppressed. If a telescope cell triggers, we aim to read out all its telescopes, independently of whether they themselves triggered or not. Even if the light intensity in a neighboring telescope is too low to cause a trigger, Monte-Carlo studies [10] show that its data is valuable for the shower reconstruction.

1.5 Readout Electronics

The wish to read out untriggered telescopes implies that the telescope signals are stored over the time period required to generate the coincidence trigger - up to 2 μs, depending on the distance between telescopes, their orientation, and the trigger conditions. Therefore, we plan to use for the readout either fast Flash-ADC converters or analog storage of the signals in switched-capacitor arrays, followed by slower ADCs. While the performance simulations are conservatively based on 120 MHz sampling of the analog signals (as used presently in HEGRA), we hope to achieve 250 MHz to 300 MHz sampling rate, resulting in shorter effective integration times, reduced sky noise, and improved time resolution.

1.6 Data Acquisition System

The data acquisition (DAQ) system will be similar to the system used presently for the HEGRA telescopes, based on the VME standard, with some custom-designed modules. Most of the modules originally developed for HEGRA can be used. Telescopes will be controlled and read out by local VME CPUs. The data transfer to a central event builder CPU will most likely use existing UDP-based tools, and Fast Ethernet as a hardware layer.

1.7 Monitoring and Control

All system telescopes can be controlled either locally or from a single terminal in a central station. Watchdog utilities will permanently monitor telescope operating parameters, such as PMT currents and rates, the performance of the various trigger levels and of the DAQ system, and the quality of the data, and alert the shift crew in case of problems. Calibration and monitor systems will also include laser gain calibration systems, and automatic monitoring of telescope pointing and mechanical distortions by TV cameras observing stars and calibration lights.

2 Telescope Optics

In this sections, we review the considerations relevant for the geometry of the reflector. Given the number of IACTs planned, one can afford to use custom-designed and optimized dish structures, so there is considerable freedom in the size and arrangement of the mirror tiles.

2.1 Requirements

The mirror has to intercept a sufficiently large number of Cherenkov photons and image them onto the camera. The requirements on the mirror include

- The telescopes should provide a threshold of 100 GeV. At 2 km height, a 100 GeV shower provides about 10 photons/m^2, or 1.5 photoelectrons/m^2, given typical values for the mirror reflectivity and the PMT photoefficiency. At least 100 photoelectrons are required for a reasonable image analysis, resulting in a net mirror area of about 70 m^2.
- The point spread function provided by the mirror should be smaller than, or comparable to the pixel size. The minimal pixel diameter envisioned is $0.15°$ (see discussion below), hence the image of a point light source at infinity should have a (projected) rms width of $0.05°$ or less, in order to be reasonably contained within a pixel.
- Since extended sources will be a prime target, the imaging properties should be reasonably homogeneous throughout the field of view, with its diameter of about $4°$.
- The dispersion of photon arrival times caused by different light paths in the mirror should not exceed the intrinsic width of the Cherenkov light pulse of a gamma-ray shower - about 3 ns.

Additional constraints arise from cost considerations and practical or operational issues:

- A short focal length is desirable. Increased focal length translates into increased size and weight of the camera - an issue in particular since the camera is anyway big, due to its large field of view. Support of the camera becomes increasingly difficult with larger focal lengths, and the frequencies of the lowest eigenmodes tend to decrease.
- The mirror should be segmented into relatively small mirror "tiles";. At present, the cost of mirrors increases rapidly for sizes beyond 50 cm to 60 cm, and the number of potential suppliers for larger sizes is very limited.
- The individual mirror tiles should be spherical, to simplify production and to limit costs. It would be advantageous if all mirrors had the some focal length; however, given the large number of mirrors required, one could also think of a few different focal lengths.

Since it combines very different constraints such as optical quality, mechanical issues, and cost, the optimization of the mirror geometry is nontrivial, and may require compromises in some areas.

2.2 Basic Mirror Geometry

For the reasons outlined above, almost all large Cherenkov telescopes use a mirror dish composed of many smaller spherical mirrors, with focal lengths of the order of the dish diameter, $d \approx f$ ($\pm 20\%$). The Davies-Cotton design [8] has early been proposed for the arrangement of the mirror tiles; the properties and optimization of such mirrors have been discussed extensively [11, 12, 13]. Best focusing for on-axis rays is obtained if the individual mirrors (of focal length f, and hence radius of curvature $r_{mirror} = 2f$) are arranged on a sphere of radius f, with their axes pointing at a spot on the optical axis of the telescope at a distance $2f$ from the point where the optical axis intersects the mirror dish (see Fig. 3). This arrangement simply reflects the fact that the average focal surface for a spherical mirror is itself a sphere of radius f, and that hence the distance of all tiles from the camera should be identical. For light incident on the optical axis, the image size is essentially governed by the imperfections of the mirror tiles, which in the following were assumed to provide a focal spot of 1 mrad (diameter containing 80% of the light).

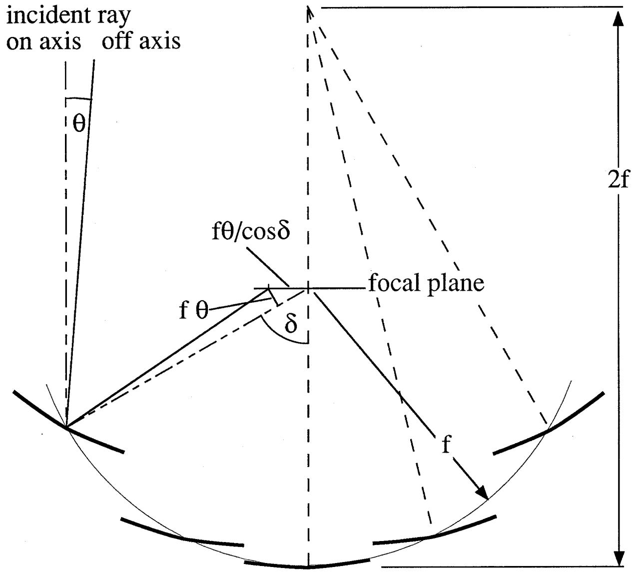

Figure 3: *Basic Davies-Cotton mirror geometry, illustrating image formation for on-axis, and for off-axis rays at an angle θ relative to the optical axis.*

Cherenkov telescopes require a rather large field of view compared to conventional optical telescopes, or solar concentrators (the original application of the Davies-Cotton mirror). For off-axis rays, the imaging properties deteriorate rapidly, as illustrated in Figs. 4 and 5, which show the size of the focal spot as a function of the angle of incidence θ, derived using a simple ray-tracing program. The main reason is that in the camera plane, a mirror which is viewed under angle δ from the camera generates an image which is enlarged by a factor $1/\cos\delta$ (see Fig. 3); the superposition of images of different scales smears the image. Averaging in δ and azimuth over the entire mirror surface, one finds that the rms width of the image increases linearly with the angle of incidence θ, and quadratically with the angle $\delta_{max} \approx d/2f$. Another aspect is that for non-zero θ the best focus for each tile is obtained in front of the camera plane. However, given the small mirror tiles considered, and the resulting large depth of focus, this effect is only of secondary importance.

Options to improve in particular the imaging for off-axis rays will be discussed later in this chapter; some improvements are possible, but they are relatively modest and involve other complications. As a design base line, we therefore stay with the Davies-Cotton design. The individual mirror tiles are round, with 50 cm diameter. The size is governed largely by cost reasons; including the costs for alignment and support, mirrors of this size presently seem to offer the lowest cost per area. In total, 420 such mirrors (Fig. 20) result in a mirror area of 82 m^2, providing a small extra margin over the minimal size required, partly to compensate for effects such as the shadowing of the mirror by the camera masts. The outer contour of the mirror dish is a hexagon, with a (flat-to-flat) size of about 11 m.

To simplify installation and alignment, we consider grouping the 50 cm mirror tiles into clusters of 7, each cluster forming a rigid and pre-aligned mechanical unit. The most convenient solution is to make all clusters identical and adjust the mirrors of a cluster such that their surfaces coincide with a sphere, making them equivalent to a single larger spherical mirror. Such a mirror is illustrated in Fig. 6. As will be shown below, this solution results in a slight degradation of optical quality compared to a mirror where individual tiles follow a Davies-Cotton layout.

An alternate arrangement would use four different types of clusters corresponding to the four 'rings' of clusters, each type with different relative adjustments of the tiles, and would thus recover the full optical performance while retaining most of the simplicity in the sense that clusters are not 'individuals', but can be manufactured and adjusted in series.

2.3 Factors Governing the Optical Quality of the Mirror

The optical quality of a Davies-Cotton mirror is governed by three factors:

- The ratio of focal length to diameter, f/d, see Fig. 7. For $d \approx 11$ m, a focal length of 14 to 15 m would

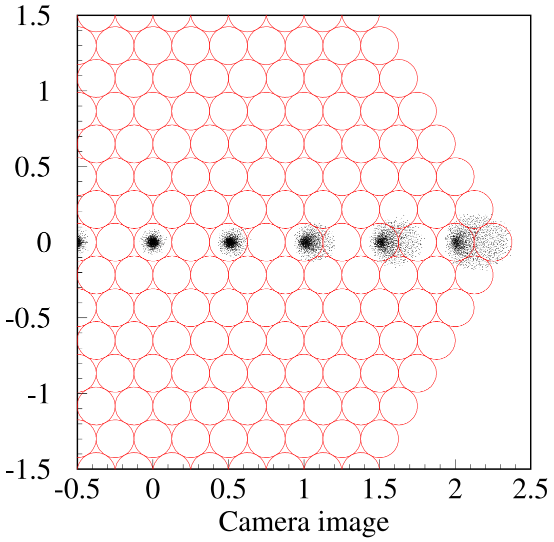

Figure 4: *Simulation of the images generated by point light sources at infinity, for a tiled 82 m^2 Davies-Cotton mirror with 12 m focal length. The individual mirrors are assumed to provide a 1 mrad spot size (diameter for 80% containment). Superimposed is a 271-pixel camera with 0.25° pixel diameter.*

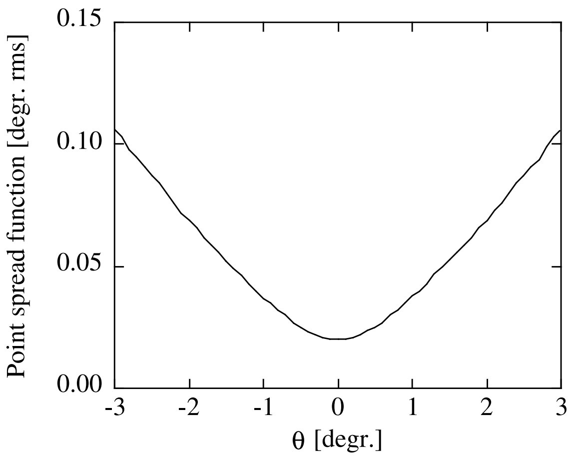

Figure 5: *Rms width (in the "long" direction, i.e, radially) of the image generated by a point light source at infinity, as a function of the angle of incidence, for a tiled 82 m^2 Davies-Cotton mirror with 12 m focal length and 1 mrad spot diameter of the mirror tiles.*

be required to maintain a 0.05° spot size over the entire field of view. Mechanical constraints concerning the stability of dish and camera support, on the other hand, favor smaller focal lengths.

- The optical quality of the individual mirror tiles. We characterize tile quality by the diameter of a circle enclosing 80% of the image for parallel incident rays. For a Gaussian intensity profile, the typical quality figure of 1 mrad corresponds to a (projected) rms width of the spot of 0.28 mrad. Fig. 8 illustrates the influence of mirror quality.

- The effective size of the individual mirror tiles. For the Figures 7 and 8, the individual tiles were assumed to be of negligible size. Finite-sized tiles introduce additional imaging errors, see Fig. 9. With the large

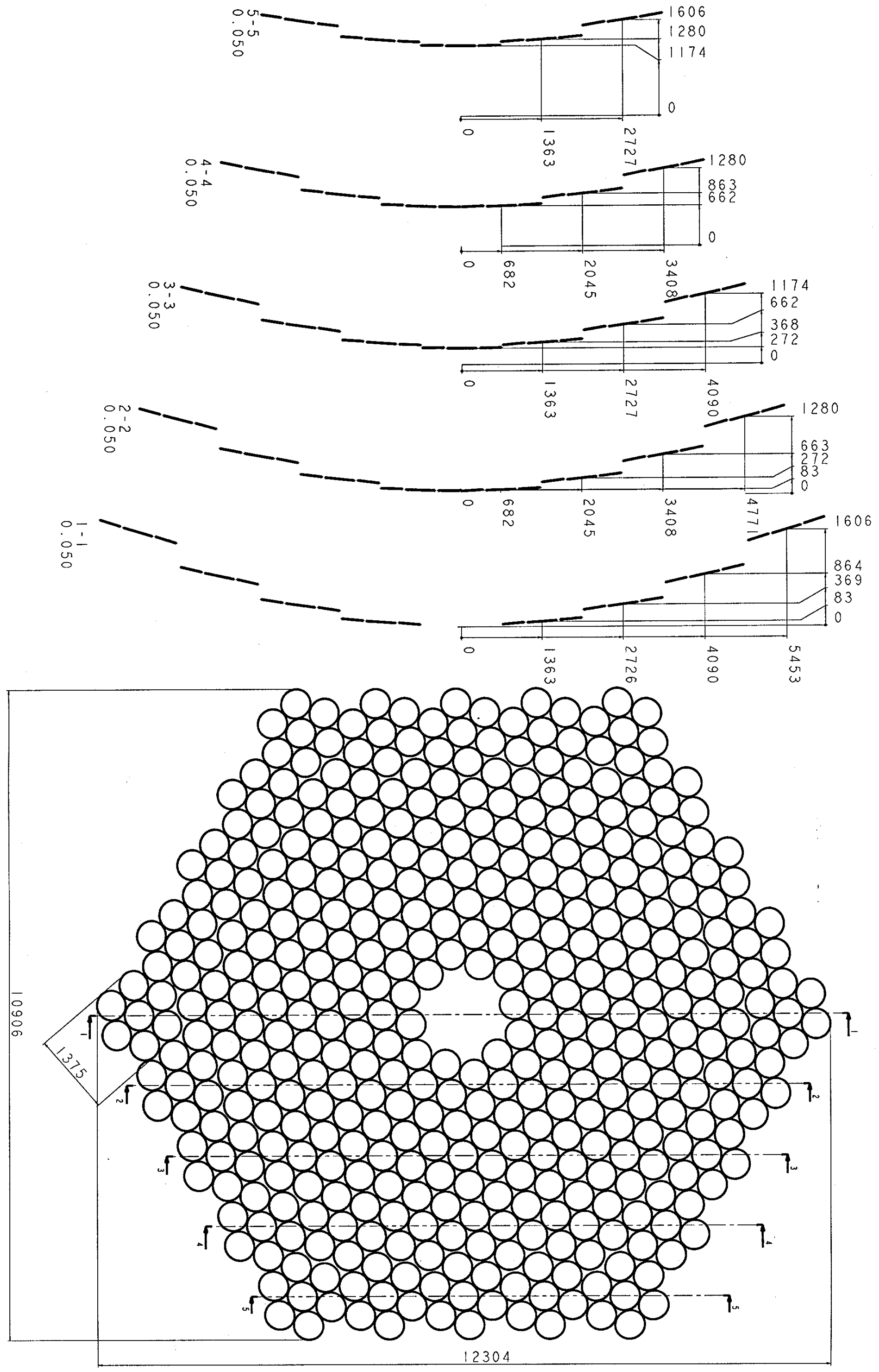

Figure 6: *Cross sections through the mirror surface, illustrating how the tiles are combined into spherical clusters, with clusters following a Davies-Cotton layout (dimensions in mm).*

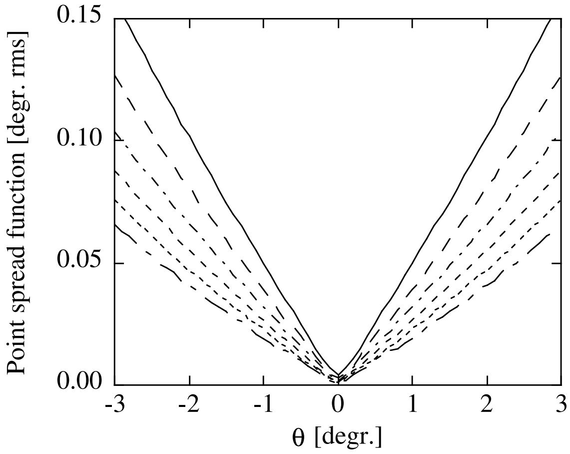

Figure 7: *Rms width (in the "long" direction) of the image of a point light source at infinity, as a function of the angle of incidence, for different focal lengths of 10, 11, 12, 13, 14 and 15 m (top to bottom). Individual mirror tiles are assumed to be small perfect spherical mirrors, and are mounted in a Davies-Cotton fashion.*

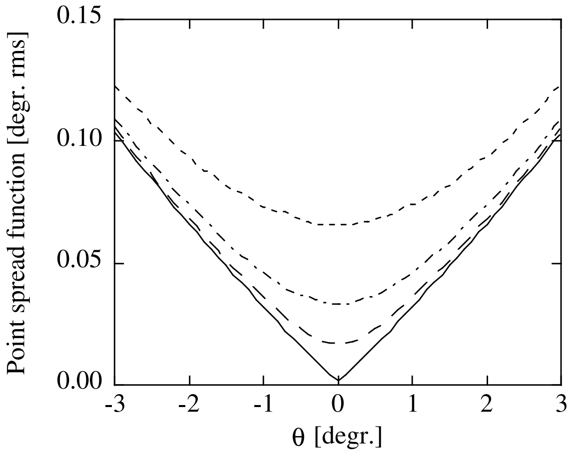

Figure 8: *Rms width (in the "long" direction) of the image of a point light source at infinity, as a function of the angle of incidence, for 12 m focal length, and a spot size of the small individual mirror tiles of 0, 1, 2, and 4 mrad (bottom to top, defined as the diameter of a circle enclosing 80% of the image intensity).*

tiles - equivalent to a cluster of 7 mirrors combined to form a spherical surface - degradation is noticeable.

As far as timing is concerned, all variants show a spread of photon arrival times which is almost independent of the angle of incidence, and varies between 1.5 and 1.2 ns rms for focal lengths between 12 and 15 m. While this spread is certainly not negligible compared to the width of the light pulse, we consider it acceptable.

2.4 Choice of Mirror Parameters

The final choice of mirror parameters represents a compromise between performance and cost as far as the optical quality of the mirror tiles is concerned, and between performance and mechanical complexity (and cost) as far as the focal length and the arrangement of mirrors within clusters is concerned. Of course, the various choices are interrelated; it does not help to optimize one aspect and to ignore the others. Fig. 10 illustrates some of the relevant combinations of mirror quality, focal length, and cluster arrangement. We consider $f = 12$ m as the minimal acceptable focal length; 14 m to 15 m are required to achieve the 0.05° spot size over the entire field of view. (Since much of the initial design work has been carried out with $f = 10$ m, some of the technical illustrations of the telescopes - such as Figs. 1, 20, 6 - still refer to this shorter focal length.)

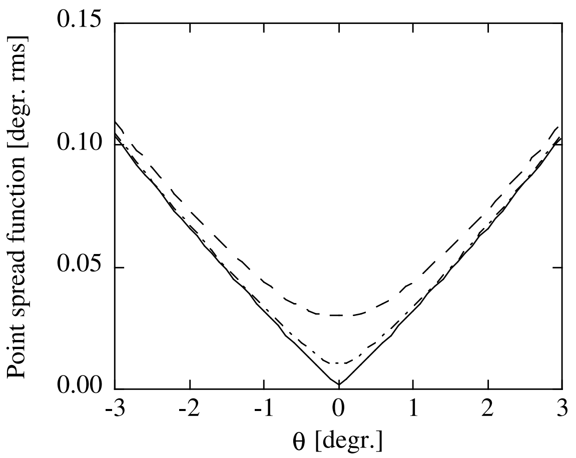

Figure 9: *Rms width (in the "long" direction) of the image of a point light source at infinity, as a function of the angle of incidence, for 12 m focal length, and perfect spherical mirror tiles. Lines correspond to very small tiles (bottom), 50 cm diameter tiles (middle), and clusters made of 7 tiles of 50 cm diameter forming a larger spherical mirror (top).*

Parameter	minimal solution	optimal scenario
System focal length	12 m	15 m
Cluster configuration	1 cluster type,	4 cluster types,
	spherical surface	Davies-Cotton geometry of tiles
Tile/cluster focal length	all identical	different for each cluster type

Table 1: *Major design choices concerning mirror geometry. See section on "Improved mirror geometries" for last item.*

Concerning the mirror tiles, it appears that mirrors with a 1 mrad focus (80%) can be mass-produced at modest additional cost over the lower-grade mirrors used e.g. in solar concentrators. We therefore use a 1 mrad spot size as a baseline. Whether mirrors can be combined into identical spherical clusters, or whether the arrangement of mirrors within clusters has to vary with cluster radius depends much on the focal length finally chosen; the shorter the focal length, the more the detailed arrangement matters. For $f = 15$ m, performance differences between the two variants are small, and one may well opt for the simpler variant of identical clusters,. For $f = 12$ m, differences are noticeable, and for $f = 10$ m they are dramatic. At such shorter focal lengths, optimized clusters are preferred.

A simulation of the optical quality in the optimal scenario - 15 m focal length and 1 mrad mirrors - is illustrated in Fig. 11; superimposed is a camera with 0.15° pixels.

The options for the mirror geometry are once more summarized in Table 1; a decision will be taken once the study of the mechanical constraints is further advanced.

2.5 Improved Mirror Geometries

With the large field of view of the planned telescopes, the deterioration of image quality with increasing angle of incidence θ is of serious concern. The most efficient cure is clearly a large focal length. However, practical considerations impose severe limits on f. From the discussion given above, two other measures might help:

- Adjustment of the relevant geometry parameters, such as the pointing of the mirrors in the outer rings or the location of the focal surface, to improve imaging for off-axis rays in a certain angular range. Any such measure will necessarily spoil the on-axis response to some extent.
- Use of mirror tiles with different focal lengths in each 'ring' of mirrors, to compensate for the differences in image scales.

As an example for the first option, Fig. 12 illustrates that the off-axis imaging is indeed improved a bit by moving image plane forward towards the mirror by a few cm. With a planar camera surface, the on-axis

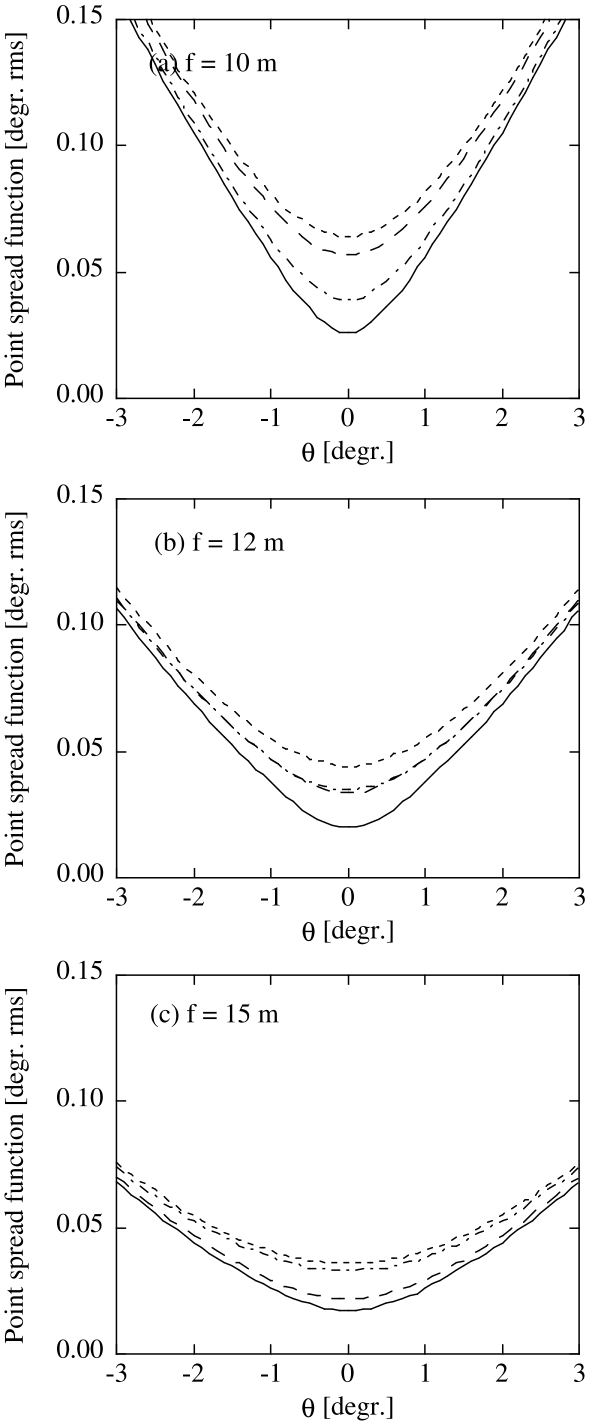

Figure 10: *Rms width (in the "long" direction) of the image of a point light source at infinity, as a function of the angle of incidence, for 10 (a), 12 (b) and 15 m (c) focal length, for individual mirror tiles with 1 mrad focus (full lines), for spherical 7-mirror clusters of 1 mrad mirrors (long-dashed lines), for individual 2 mrad tiles (dot-dashed lines), and for clustered 2 mrad mirrors (short-dashed lines).*

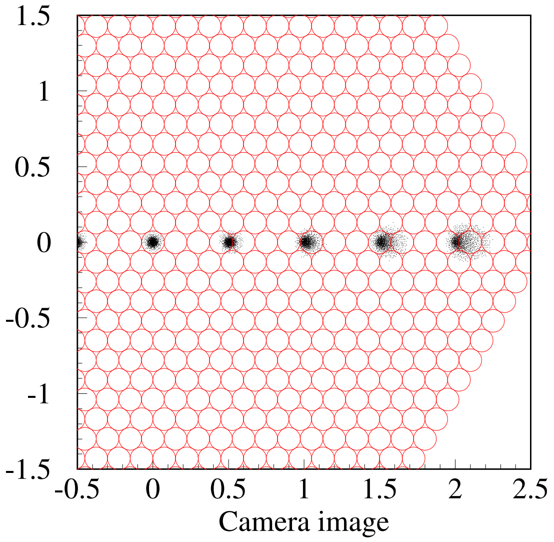

Figure 11: *Simulation of the images generated by point light sources at infinity, for a tiled 82 m^2 Davies-Cotton mirror with 15 m focal length. The individual mirrors are assumed to provide a 1 mrad spot size. Superimposed is a camera with 0.15° pixel size.*

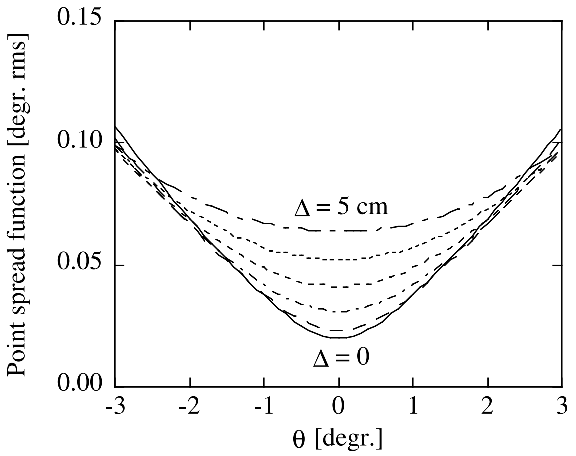

Figure 12: *Rms width (in the "long" direction) of the image generated by a point light source at infinity, as a function of the angle of incidence, for a tiled 82 m^2 Davies-Cotton mirror with 12 m focal length and 1 mrad spot size of the mirror tiles. The spot width is shown in the nominal focal plane, and in planes displaced towards the mirror by Δ = 1, 2, 3, 4 and 5 cm compared to the nominal plane.*

imaging deteriorates, of course. A spherical camera surface would provide the best imaging; however, the gains are so minute that they do not seem to justify the increased mechanical complexity. On the basis of ray-tracing simulations we have furthermore systematically varied the dish shape, trying to minimize the spot size, averaged over the field of view. The parameters of the "optimum" dish (using tiles of a single focal length) were virtually identical to the Davies-Cotton design. On-axis imaging of the outer mirrors is improved very slightly if they are moved forward by a few cm. However, the resulting change of the overall spot size is barely noticeable; off-axis imaging is not improved at all.

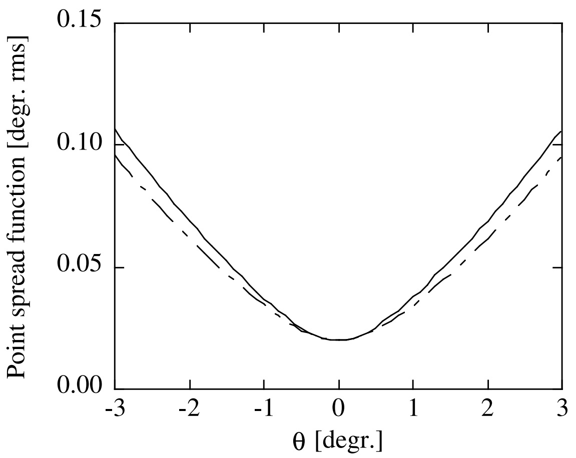

Figure 13: *Rms width (in the "long" direction) of the image generated by a point light source at infinity, as a function of the angle of incidence, for a tiled 82 m² mirror with 12 m focal length and 1 mrad spot size of the mirror tiles. The full line represents a Davies-Cotton design with identical focal lengths of all tiles, the dashed line a design where the focal length is shortened for the outer mirrors, as described in the text.*

More can be gained by varying the focal lengths of mirrors as a function of tile location, in order to partly compensate for the variation with δ of the image spot, and to reduce the resulting smearing. According to Fig. 3, a beam of light incident at an angle θ with respect to the optical axis of the telescopes is imaged by a given mirror tile at a point x in the camera plane

$$x \approx f\theta/\cos\delta \approx f\theta(1+\frac{\delta^2\cos^2\phi}{2}) \quad .$$

Here, ϕ is the azimuthal angle (viewed along the telescope axis) between the incident light and a mirror tile. Reducing the focal length for each "ring" of tiles (tiles with the same or similar δ) by a factor $1/(1+\delta^2/4)$ will at least guarantee that the average image point is the same for each ring. Of course, the mirrors need to be moved forward compared to the Davies-Cotton layout, to a point where the distance to the camera is again $f(\delta)$. However, both the analytical estimate and the explicit ray-tracing (Fig. 13) show that the gain is limited; the increase of spot size with θ is reduced by about 10% to 15%.

In summary, the only promising option to improve imaging seems to vary tile focal length with tile location; even there, the improvement is modest. In our baseline optics design we assume identical focal lengths of all mirrors. However, unless more detailed studies indicate serious problems concerning logistics or production, a solution with a (small) number of different matched focal lengths would certainly be preferred.

In trying to improve telescope optics, one could also think about multi-mirror designs, such as Cassegrain or Gregorian optics with a secondary mirror. Such systems have the feature that the camera can be located in the plane of the dish, with potential benefits in the form of shorter cables, improved access, etc. A two-mirror design allows to compensate imaging errors to a much higher degree than possible with a single mirror; particularly interesting is the - otherwise rarely used - Gregorian design with a spherical main mirror, in our case composed of spherical mirror tiles. We have not followed these lines further because of various reasons, such as:

- Two-mirror telescopes tend to have rather long effective focal length; we found it difficult to reduce the focal length below about twice the focal length of a single-mirror design. With such a large focal length, pixel sizes increase into a region where it is difficult to find suitable inexpensive PMTs.

- The secondary mirror is a non-trivial object, both in its size and required quality. Manufactured with conventional technology, it would most likely dominate the cost of the telescopes.

2.6 Strategy for Mirror Alignment

For optimum performance, mirror tiles need to be aligned individually to compensate tolerances in the support structure, as well as variations in the mirror focal lengths. The precision of the support structure is in the range of some tens of millimeters in case of the dish, and of the order of 1 mm for the cluster frame (in either case, the stability is of course much better). Without special selection, mirror tiles tend to exhibit focal length

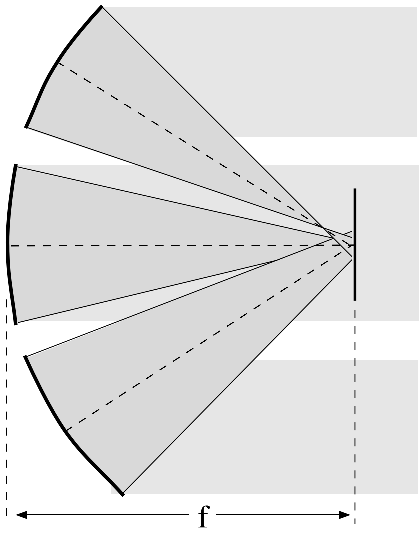

Figure 14: *Alignment of mirror tiles within a cluster. The focal lengths of the tiles vary from tile to tile. Not drawn to scale.*

variations of the order of 1%. The strategy for mirror alignment and control is obviously a key ingredient for the performance of the telescope, and must be a basic part of all design considerations.

In our present telescope design, alignment is divided into two steps:

- The alignment of mirror tiles on their cluster frames, such that each cluster provides an optimal focal spot. This alignment occurs once during fabrication (or refurbishing) of the clusters, in a controlled environment.
- The alignment of mirror clusters on the mirror dish, which occurs in the field. Given the nontrivial access to the mirror dish, and the need to monitor and if necessary re-adjust the optical quality of the telescope periodically, we plan for this second task to install remote control systems for each mirror cluster, and to provide automatic procedures for standard alignment tasks.

This division limits the number of parameters for the field adjustment.

The requirements on the precision are similar in the two cases: the contribution of alignment errors to the image spot size should not spoil the intrinsic imaging quality of the mirrors (1 mrad spot diameter). This implies that the orientation of mirrors is correct to better than 0.25 mrad. Deviations in the distance of the mirror from the focal plane, or equivalently deviations between the actual and the nominal focal length are much less critical. Because of the relatively modest size of the mirror tiles, a 1% deviation in focal length (or focal distance) implies at the nominal focal distance an image disk with a diameter of 1% of the tile diameter, equivalent to 5 mm or 0.4 mrad (for$f$ = 12 m). One will therefore not try to compensate mirror-by-mirror variations in focal length - anyway a difficult task, given that a 1% adjustment in focal length would imply displacement of the mirror of more than 10 cm. Rather, the 7 mirrors of a cluster will be aligned such that their images superimpose at the nominal focal distance (Fig. 14). Each of the clusters then behaves like a not-quite-ideal mirror with exactly the nominal focal length. If, due to mechanical tolerances of the dish, the distance of the cluster from the camera does not coincide with the the nominal focal length, one cm deviation causes an image disk size of only about 0.1 mrad.

In summary, alignment needs only to be concerned with the orientation of the mirror tiles and clusters, but not with their distance to the focal plane.

A second issue is under which conditions the mirror should be aligned. The clusters are designed as rigid mechanical units, with negligible deformations under load. Therefore, alignment can proceed in the lab without regard for the final location or orientation of the mirror. Sufficiently precise alignment can be obtained with a light source at twice the focal distance. The mirror dish, on the other hand, does deform noticeably under load. Fig. 15(a) shows the change in orientation of some characteristic mirror clusters under the influence of gravity, as a function of the elevation. Clusters tilt by as much as ±0.3 mrad between 10° and 90° elevation. The influence of deformations can be reduced by aligning the mirror at an elevation near its typical working point. An alignment at 50° will reduce deformations to ±0.1 mrad for elevations between 20° and 90° (Fig. 15(b)). If observations concentrate on the range between 45° and 90° elevation, as with most present Cherenkov telescopes,

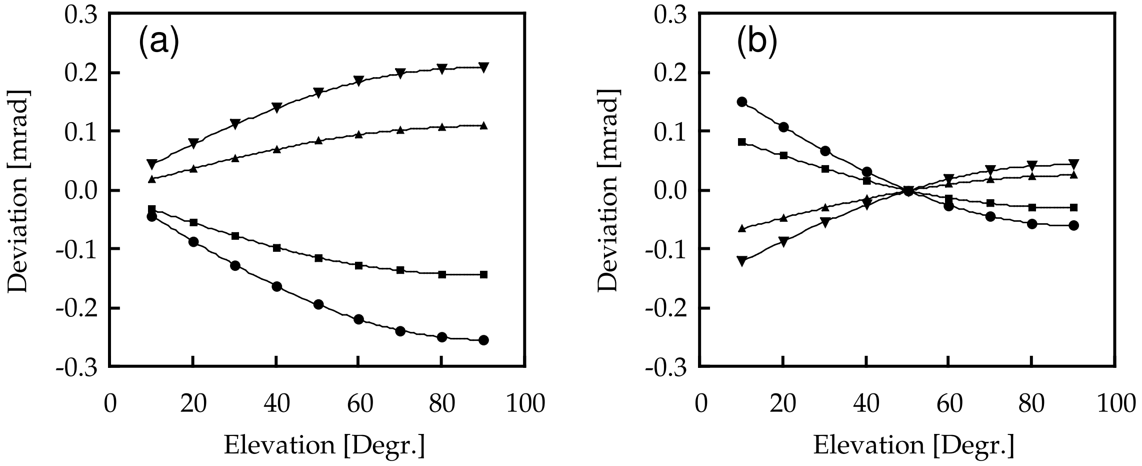

Figure 15: *Change in cluster pointing on the dish due to the influence of gravity, as a function of elevation angle, for several typical clusters mounted on the space frame. (a) Relative to the undistorted dish without load, (b) for a mirror aligned at* 50° *elevation.*

alignment at 70° will reduce errors by another factor of two. Such a procedure implies, however, that the mirror cannot be aligned in the position most convenient for access, and that it is difficult to use external alignment jigs such as light sources etc.

For this in-situ remote adjustment of the mirror clusters, various options exist, such as:

- Remotely actuated laser pointers connected rigidly to the cluster frame can be sensed either by the camera pixels themselves, or by CCDs or multi-anode PMTs in the center at the camera and/or near the outer edge. Using the pixels themselves, sufficient resolution is achieved by moving the cluster to scan the laser across the boundary between two pixels; the adjustment motors have to work reproducibly enough to move the cluster from this reference position to its nominal position, with the laser pointing somewhere inside the pixel. An alternative is to widen the beam, such that a reliable center of gravity can be derived from the currents of adjacent pixels. The advantage of the laser pointer technique is that a fast check of the mirror adjustment is possible. However, image quality is not checked directly; one has to rely either on a very precise and stable a priori adjustment of the pointer, or provide a second technique for calibration. We note further that the laser cannot point along the optical axis of the mirror (it will miss the camera), and that therefore a single beam cannot unambiguously determine the orientation of a cluster.

- Adjustment using the images of bright stars, again preferentially based on CCDs or multi-anode PMTs which are either integrated into the camera, or can be moved in front of the camera (in the latter case, a small mirror would be used intercept the beam and deflect it by 90° into the detector, such that the detector surface is at the correct distance from the mirror). If the dynamic range of the detector is sufficient, the contribution of a single cluster can be isolated by detecting how the overall image varies as with the pointing of this cluster. An alternative method to isolate contribution of a single cluster to the image consists in tilting all other mirrors away by a few times the image size. To adjust all mirrors, one would tilt all the mirrors away, then, one-by-one, tilt one mirror in, adjust its orientation, memorize the positions of the actuators, tilt it away and move to the next mirror. At the end, all mirrors are moved to their optimal positions. This method again requires the mirror drives to be reproducible on the scale of the image size. Compared to the alignment with laser beams, this technique requires more time - on the scale of a minute per mirror cluster - but it optimizes the point spread function directly, without further assumptions.

We envision to use the second technique - star images - for the initial calibration, and for occasional follow-ups, but also to install the inexpensive laser pointers in order to allow quick checks. The central pixel of the camera may be replaced by a CCD array or a multichannel PMT with small pixels, and similar elements should be installed at the periphery of the camera. The mirror actuators need to be reproducible on the scale of $\approx$100 μm for travel over short distances ($\approx$ 5 mm); the precision requirements for longer paths are relaxed. Suitable commercial drives are available at modest cost; one could use e.g. a stepper motor driving a spindle.

Source	Spot size [mrad rms]	Comment
Contributions related to mirror tiles		
Tile point spread function	< 0.28	specification
Focal length variations (1% rms)	< 0.10	specification
Deformation under gravity/wind load	0.03	calc. for aluminum mirror
Deformation due to temperature and temp. gradients	< 0.02	calc. for aluminum mirror
Contributions related to mirror clusters		
Deformation of cluster frame under gravity/wind load	0.1	(see caption)
Deformation of cluster frame due to temp. effects		expected to be small
Alignment of tiles within cluster	0.20	estimate
Contributions related to mirror dish and camera support		
Deformation of dish under gravity/wind load		
- changes in cluster orientation	0.3	finite elem. calc.
- changes in cluster location (focal distance)	< 0.01	finite elem. calc.
Deformation of dish due to temperature gradients		expected to be small
Alignment of orientation of clusters	0.20	estimate
Non-alignable imperfections in dish shape (1 cm)	0.03	typ. manuf. tolerance
Camera alignment relative to focal plane (0.5 cm)	0.10	estimate
Total	0.53	

Table 2: *Contributions to the size of the image of point source at infinity, on the telescope axis. Values given refer to* projected rms *spot width, and are based on specifications for the various elements, on finite element simulations, and partly on guesses based on past experience. The value for the mechanical rigidity of a cluster is a target number; the present design (discussed later in the text) does not quite meet the goals. The numbers assume $f = 12$ m.*

2.7 Optics Error Budget

The final imaging performance of a telescopes is governed by a combination of factors relating to the quality of the image tiles, the aberrations of the mirror as a whole, the mechanical stability of the dish, alignment errors etc. In Table 2 the present estimates for the various contributions are summarized. The values represent our present knowledge; details concerning some aspects of the mechanics are given in the following sections of this Appendix. The numbers in the table refer to *rms* variations in a *projection* of the image onto one of the axes of the camera coordinate system. Of course, the intensity distributions generated by imaging errors are frequently not Gaussian. In cases where the exact distribution is known, such as for deviations in the focal length, the appropriate rms width was calculated. In other cases, such as for the point spread function of the tiles, a Gaussian distribution is assumed.

We note that, unlike for optical telescopes, the quality of the tracking does not enter into the error budget. Since the "exposure time" of Cherenkov images is so short, tracking errors do not matter, provided that the actual pointing of the telescope is known. Therefore, relatively simple drive systems can be used, if combined with shaft encoders of sufficient quality.

The net effect of all imperfections is roughly equivalent to a doubling of the point spread function of the individual mirror tiles; the effective imaging properties are therefore approximately described by the curves referring to 2 mrad mirror tiles (diameter for 80% containment) if Fig. 10. In particular for $f = 15$ m, the mirror provides a rather uniform imaging, with a point spread function of less than $0.05°$ rms over most of the field of view; slight improvements at large angles are still possible by the measures discussed earlier.

3 Mirror Tiles

3.1 Requirements

Some of the requirements concerning the individual mirror elements have already been given in the previous section; these concern in particular

- Size: an upper limit on the mirror size is given by the quality of the Davies-Cotton optics, which deteriorates rapidly with increasing size of the mirror tiles. Also, requirements concerning deviations in focal length become more stringent for larger mirrors. A mirror diameter of about 1.5 m is certainly the upper limit. Since the number of mirror tiles increases with the square of the radius, a lower limit on mirror size is determined by the number of tiles and the associated number of adjustment elements; significantly smaller diameters than the 0.5 m used in the baseline design are hard to imagine. Within these limits, the choice is dictated by economics.

- Focal length: the mirror should provide a focal length of 12 m or 15 m with a tolerance of not more than 1% rms (or a maximum deviation of 1.7%, if specified this way). For a 50 cm diameter mirror, this implies a precision of about 10 μm for the sagitta.

- Point spread function: 80% of the light should be contained in a circle of 1 mrad diameter, equivalent to a (projected) Gaussian point spread function of 0.28 mrad rms. Given that at least for off-axis rays other factors quickly dominate the image width, this condition could be relaxed somewhat, should this result in significant savings or simplifications.

The requirement concerning the point spread function - 80% of reflected light within one mrad - implies a smoothness of the surface on both macroscopic and microscopic scales; on macroscopic scales, surface errors with a characteristic length scale L must not exceed an amplitude $A \approx 10^{-4}L$. A surface roughness σ_s on microscopic scales introduces a diffuse component of reflection; the specular reflectance of a rough surface is [15] $R_s \approx R_0 \exp\left(-(4\pi\sigma_s/\lambda)^2\right)$, where R_0 is the reflectance of a perfect surface. To maintain 80% specular reflectance at 300 nm, surface roughness should be less than about 10 nm.

There are quite a number of additional considerations influencing the choice of the mirror elements:

- Wavelength region: atmospheric transmission cuts off the Cherenkov spectrum at 300 nm; light yield at shorter wavelengths fluctuates strongly with the height of the shower maximum. Therefore, normal PMTs with Borosilicate glass windows are most appropriate, since they cut off rather sharply at about 300 nm. Given the spectral sensitivity of Bialkali photocathodes, the highest photoelectron yield is reached in the 300 nm to 400 nm region, and useful output is obtained up to 600 nm. The mirrors should therefore provide high reflectivity between 300 nm to at least 600 nm. This requirement leaves only aluminum as a suitable reflector material.

- Reflectivity and lifetime: ideal aluminum films have a reflectivity of about 92% in the relevant wavelength range. However, unprotected aluminum reflectors are short-lived, in particular in IACT applications, where mirrors are fully exposed to weather and dust at least during the observation periods. With a large system like the one discussed here, mirrors should live a few years before they need to be replaced or refurbished. Protective treatment will in general reduce the reflectivity, unless special multi-layer coatings are used. The goal should be to maintain an initial reflectivity of at least 85%. However, in the end the quality of the system is determined by the average reflectivity over the years, and a stable 80% mirror is superior to one which starts off at 90% and drops to 70% after a year!

- Mechanical stability and support: to simplify support and alignment, a mirror tile will be supported in only three points (optical multi-mirror telescopes usually have more sophisticated mirror supports). The mirror needs to be stable under the varying gravitational loads.

- Thermal stability: radiative cooling as well as environmental influences can induce temperature differences ΔT between the front and rear surface of a mirror tile, resulting in bending and a change in focal length, $\Delta f/f = 2\alpha\Delta T f/h$. Here, α is the coefficient of expansion and h the thickness of the mirror. For aluminum mirrors, the mirror temperature needs to be homogeneous within a few tenth of a degree. As long as the mirror is made of bulk aluminum with its good heat conductance, temperature uniformity is trivially obtained; however, the point needs consideration, e.g., for mirrors with honeycomb structures sandwiched between thin front and rear cover plates.

- Recovery: assuming that mirror reflectivity will deteriorate on a scale of several years, and that the cost of the mirrors is not insignificant, a technique and facilities must exist to refurbish mirrors at rate such that one can keep up with the rate of deterioration. In practice, one would most likely keep a spare set of mirrors, so that all telescopes remain active while one set of mirrors after another is refurbished.

- Weight: in zeroth approximation, the weight of the telescopes scales with the mirror weight, and one should attempt to make mirrors as light as possible. However, survival under peak wind loads - which are larger than gravity loads - requires anyway a minimum stiffness of the dish. Components such as the drives for cluster adjustment, and the mechanics for adjustment of mirror tiles on the cluster frames do not vary dramatically with mirror weight. Simulations (discussed later) show that rather little is gained by replacing solid aluminum mirror tiles (which weigh about 8 kg for 50 cm diameter) with mirrors where much of the bulk material is removed, either by machining or by employing a honeycomb technique, resulting in a 50% weight reduction. As a consequence, mirror weight is not a prime consideration, within the range given above.

- Cost & Production: cost is obviously a driving factor in the selection of mirrors; however, another nontrivial aspect is the production of about 1700 mirrors on a scale of about two years for the initial cell of telescopes, and at a higher rate if a full array is implemented. Not all techniques are suitable for mass production on this scale, or require significant capital investment to set up production lines. Shape: a final question concerns the shape of the mirror - round or hexagonal. A hexagonal mirror will obviously provide an increase in area coverage of about 10%, resulting in a smaller dish for the same mirror area. On the other hand, hexagonal mirrors tend to be more expensive, since they are usually cut out of round mirrors. Overall, the difference in system cost is probably quite small. Our present studies are based on the assumption of round mirrors, which results in a conservative design as far as reflector area is concerned.

3.2 Options for mirror elements

The mirror types under consideration share a common structure: a substrate determines the shape of the mirror, a metal layer with high surface quality acts as reflector, and a thin transparent top layer serves to protect the sensitive reflector.

Options for the structural material include

- Glass like in the present HEGRA telescopes; suitable mirrors can e.g. be ground from thick float glass.
- Aluminum, either in bulk form or in the form of relatively thin aluminum plates strenghened by a honeycomb backing structure. Modern diamond microlathes allow to machine the aluminum to provide a reflective surface, without a special reflective coating.
- Composite materials, such a carbon fiber laminates. However, relatively inexpensive glass fiber-epoxy laminates have marginal long-term stability, and their high costs seem to exclude carbon fiber laminates for our application.
- Stretched membranes, e.g. pretensioned steel membranes of a few 100 μ thickness, formed to a paraboloid by a slight underpressure on the back side of the membrane, and covered with a suitable thin reflective layer. This technique has been developed for solar concentrators, and has evolved considerably over the last years [16]. It is not clear if this technique can provide sufficient image quality.

Mainly for reasons of cost and availability, an aluminum substrate is presently the preferred option; the machining of aluminum is less labor-intensive and costly than the grinding of glass.

As already mentioned above, the reflective layer needs to be an aluminum film, with a minimal thickness of a few 100 nm. A larger variety of choices exists for the surface protection:

- Quartz coating is a common technique for surface protection; the present HEGRA mirrors e.g. have a 1 μm Silicon dioxide coating and have demonstrated a lifetime of several years under rough conditions. Their initial reflectivity varies between about 85% at 300 nm and 90% for large wavelengths [21].
- Anodization [17] is another standard technique. For optimum reflectivity, the thickness of the anodized layer should correspond to about 1/2 wavelength, or about 100 nm. For example, the mirrors of the Whipple telescope are anodized; they maintain 92% reflectivity at 300 nm, and show a 5% drop at 450 nm [22].
- Glass sheets: while the use of thick back coated glass mirrors is problematic because of the absorption at short wavelengths (apart from the problems in shaping the glass with the required precision), thin glass sheets may provide acceptable performance combined with excellent protection. The reflective coating is applied to a thin(a few 100 μm), rather flexible glass sheet, which is then glued onto the substrate defining the mirror shape. This technique is used extensively in solar concentrators [16]. Borosilicate glasses cut off at 280 to 320 nm; folded with the Cherenkov spectrum, the net loss is less than 10%, see Fig. 16.
- Polymer films, either in form of an additional coating over a front-surface reflector, or as back-coated transparent membranes, are under intensive study for solar-energy applications. Most polymers, however, age rapidly under UV radiation, which makes them a poor choice for IACTs located at high altitude.

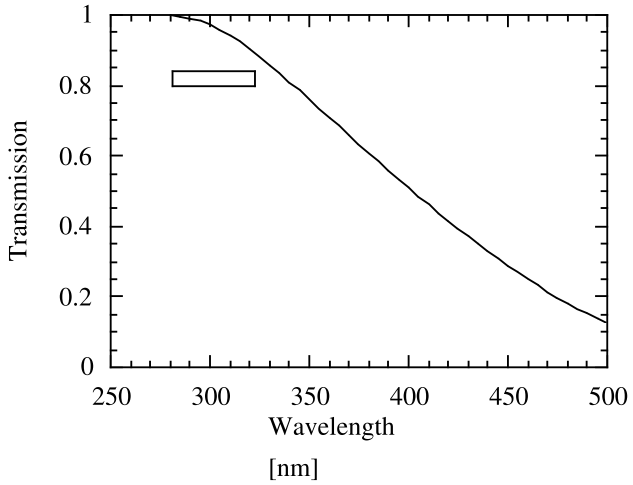

Figure 16: *Loss in photoelectron yield due to a thin glass protective layer, as a function of the short-wavelength cutoff of the glass. To derive the curve, the spectrum of Cherenkov light at the telescope was folded with the transmission of the glass and the PMT quantum efficiency. As typical for such glasses, transmission decreases from full transmission to zero over a wavelength range of about 40 nm; the cutoff is defined as the point with 50% transmission. Typical commercial glasses have cutoff wavelengths between 280 nm and 320 nm, as indicated by the horizontal bar.*

Extensive long term tests of reflector materials and protection are in progress in the solar-energy community [18, 19, 20]; but mostly preliminary results have been reported so far. The basic failure mode of quartz coated and anodized mirrors is surface corrosion starting from surface flaws. The mirrors with thin back-coated glass suffer occasionally from edge corrosion. As mentioned above, experience in the IACT community exists with both quartz-coated and anodized mirrors; mirror lifetimes tend to be sufficient, but re-aluminization is required after a few years of operation.

3.3 Aluminum Mirrors

At this point, we consider round aluminum mirrors with 50 cm diameter as the baseline option. Suitable aluminum mirrors are available from several vendors. In their simplest version, they are made from a solid aluminum substrate of about 1.5 cm thickness; the weight is about 8 kg. Cost estimates used later in this proposal are based on quotes from a Russian manufacturer. Prototype mirrors from this source (with $f = 8$ m) are under test (Fig. 17). Fig. 18 illustrates the performance of these mirrors; they meet the requirement of a 1 mrad spot for 80% light containment. The mirrors are available either with quartz coating, or anodized, or with a combination of both. Reflectivity as a function of wavelength depends significantly on the surface treatment, see Fig. 19. The anodized mirrors perform better at short wavelengths, whereas the quartz coated mirrors have higher reflectivity beyond 400 nm. Anodization followed by quartz coating combines balanced reflectivity with best surface protection, at slightly increased cost.

3.4 R&D Program

Presently, we see the following areas of R&D, which will help to decide on the final mirror technology:

- Quality control and aging tests of aluminum mirrors as the baseline option. Several mirror prototypes with different coatings will be available in the near future, and will be characterized concerning their optical properties. Aging tests are more difficult, since natural aging (hopefully) occurs too slowly, and accelerated aging tests are frequently non-trivial to interpret. One will have to rely on a combination of measurements of early variations in reflectivity, data from accelerated aging studies, as well as experience of the manufacturers, which have frequently operated mirrors outdoors for some time, e.g. in solar collectors. In particular for anodized mirrors, the aging behavior will depend on details of the anodization process and of the base material, so each type of mirror will require separate testing.

- Study of mirrors based on a back-aluminized thin glass layers. Such mirrors, e.g. on an aluminum substrate defining the shape of the mirror, would provide rather stable mirrors which can be efficiently cleaned. Open questions concern the choice of a suitable (borosilicate) glass, the sealing of the edges, and

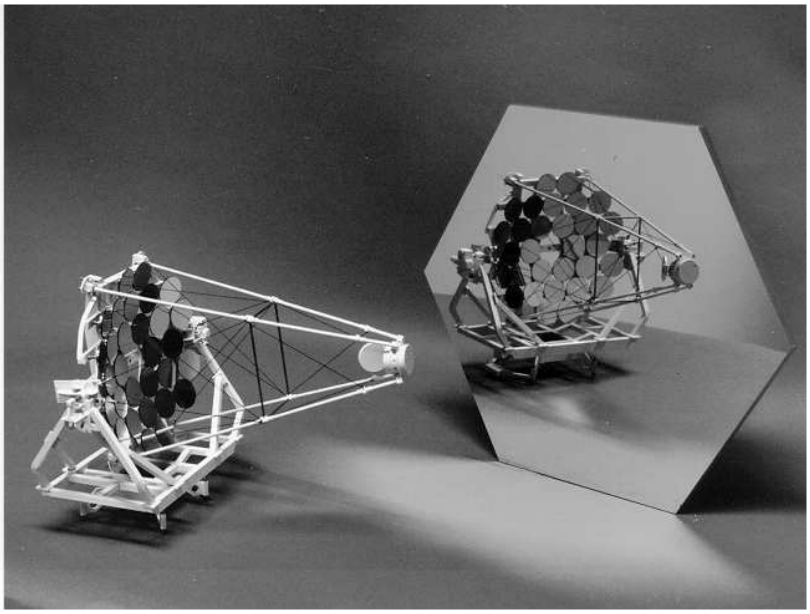

Figure 17: *Hexagonal prototype aluminum mirrors, here imaging a model of one of the HEGRA telescopes.*

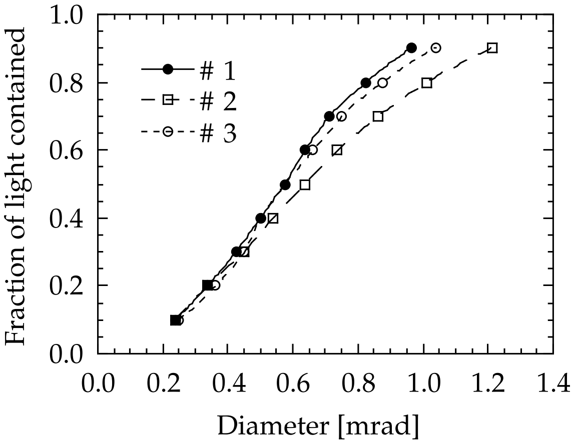

Figure 18: *Spot sizes obtained from three prototype aluminum mirrors; shown is the fraction of light contained in a circle of given diameter.*

the gluing technique to bond the glass to the substrate. In order not to spoil the optical performance, the glue layer has to be quite uniform; variations of a few μm over a scale of a cm are already critical. In this context, we will also evaluate further the potential of a stretched steel membrane as form-defining structure.

In addition, we will follow the materials tests carried out in the context of solar concentrators; first comprehensive results can be expected during 1997.

4 Mount and Mirror Dish

Purpose of mount and dish is to support and point the mirrors and the camera; the solution finally adopted for the mount and dish is primarily a question of the most cost effective design which fulfills the specifications. At this point, several options are under consideration, which differ widely in their appearance, but not in their functionality. We discuss two design studies in some detail: the space-frame dish with the modified alt-azimuth mount studied in-house, and a dish derived from the construction of communication antennas resulting from

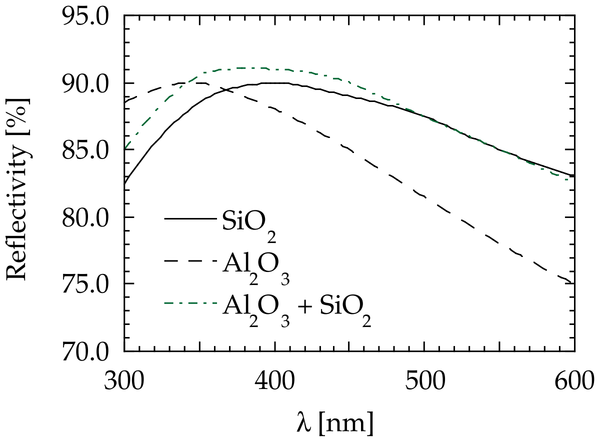

Figure 19: *Reflectivity of the prototype aluminum mirrors, for different protective coatings.*

a study by Vertex [1]. During the first half of 1997, the designs will be evaluated, and further alternatives will be considered. The detailed design will in any case have to be carried out by contractors, keeping in mind the capabilities and limitations of the final manufacturer.

4.1 Requirements

Systems of IACTs operated in stereoscopic mode reach angular resolutions of 1-2 mrad, or even better for intensive images. As a consequence, the requirements on the quality of the tracking and the stability of mount and mirror dish are larger than for individual telescopes, which have intrinsically a poorer resolution.

Requirements on the mount and dish include

- Dish diameter of about 11 m, with a focal length of 12 m (possibly 15 m), supporting 60 clusters of 7 mirrors each, with a total weight of the mirrors of about 3.5 t (1.7 t for a light-weight version of the mirrors), and of the cluster frames of about 2.5 t.
- Mirror clusters are remotely adjustable in their orientation, with a range of about $\pm 3^\circ$ in orientation.
- Under operating conditions, the dish and mirror support should be stiff enough to maintain a diameter of the focal spot of about 1 mrad (80%) for on-axis rays, in all orientations of the dish. A 1 mrad spot implies projected rms deflections of the mirror clusters of 0.14 mrad, or equivalently a maximum deflection in space of less than 0.25 mrad for 80% of the clusters.
- A camera weight of up to 150 kg must be supported at the focus; the deflection of the camera under its weight should be less than 1/2 of the minimal pixel size ($< 0.08^\circ$).
- During normal operation, tracking at the siderial rate is required, with the orientation of the telescope determined to a small fraction of the minimal pixel size ($< 0.01^\circ$). As usual with alt-azimuth telescopes, a small dead spot of about 1° around the zenith is acceptable, caused by the limited speed of the azimuthal drive.
- During the positioning of the dish, drive rates around 100°/min are required.
- The telescope should be able to point in any direction more than 10° above horizontal (with the possible exception of the above-mentioned dead spot at the zenith).
- The telescope should be able to operate within specifications up to wind speeds of 35 km/h and must survive wind speeds up to 200 km/h.
- The design should be suitable for mass production, and allow efficient assembly in the field.

[1]Vertex Antennentechnik GmbH, D-47158 Duisburg

We note that it is non-trivial to build the structure stiff enough such that the absolute pointing of the telescope is controlled to the required precision of $< 0.01°$. Bending of the camera masts alone will usually cause a deviation which is large on this scale. The solution is to aim for a pointing which is reproducible with high precision, and to use stars to derive a map for pointing corrections, which account for bending of the masts, deformations in the mount, etc. Experience with the HEGRA telescopes has shown that the required precision can be safely reached (see chapter on Monitoring and Calibration). In addition, the position of the camera relative to the dish axis will be monitored with a TV camera. To provide a starting point for the corrections, shaft encoders measuring the nominal orientation of the telescope need the full precision of about 0.01° (implying 15 to 16 bit resolution).

4.2 Option A: Space-Frame Dish

The 60 clusters of the mirror (Fig. 2) form a triangular grid. An efficient way to support these clusters is by means of a space frame with triangular cells generated by three sets of trusses crossing each other at angles of 60°, see e.g. Fig. 20. There are two options how to place the space frame relative to the mirrors. One can arrange it such that cluster centers coincide with nodes of the space frame; this is a natural choice if clusters are supported at their center. Alternatively, one can use a layout where trusses form triangles underneath each cluster, with three nodes symmetrically around the periphery of the cluster. Clusters should then be supported at corresponding points along their periphery; each node of the space frame connects to three clusters. The initial design study (Fig. 1) is based on this second option. Fig. 20 shows once more the mirror dish with its two-layered space frame. Layers are curved to match the shape of the mirror. The two layers are connected by uprights, and nodes in the upper layer are connected to nodes in the lower layers by additional diagonals to provide stiffness. Large sub-elements of the truss structure would be prepared with welded joints, and the final assembly of the dish and mount would proceed on site. Such a dish would weigh about 4 t, resulting in a total weight of dish and mirrors of 10 t.

With the aim to build the telescopes as compact as possible, to minimize weight (and counterweights), and to provide rigid support for the mirror dish and the camera, we have at this stage adopted a modified alt-azimuth mount [9] (Fig. 21). The dish is supported from three points distributed symmetrically. The altitude axis is defined by two of the support points. The third support point is moved by a linear drive. For azimuth adjustment, the whole structure rotates about a vertical axis. An alternative would be a hexapod drive system. We prefer the simpler solution with a single linear drive. The orientation of the telescope can in this case be measured in a straight-forward fashion by shaft encoders connected to the azimuth and altitude axes, and the tracking algorithms are quite similar to the ones used in normal alt-azimuth telescopes.

The design has a number of advantages over a conventional alt-azimuth mount:

- Compared to a two-point support at opposite points on the circumference, as well as compared to a single support near the center of the dish, moments and deformations are reduced.
- The camera masts emerge from the points where the dish is supported. Forces are taken by the supports, not by the dish. As a result, deformation of the dish due to moments generated by the weight of the camera is drastically reduced. A conventional mounting scheme requires extra measures to decouple camera and dish. In the CAT telescope [14], e.g., the camera masts are supported from a spider located behind the dish.
- In its horizontal position, the mirror surface is close to the ground, reducing wind load, and is readily accessible for alignment and maintenance.

A slight disadvantage of such a mount is that unlike some other alt-azimuth designs it cannot work in a 'reverse mode', with the dish and camera rotated beyond the zenith. Hence the azimuth axis has to be able to rotate at least a full 360°, or preferentially more.

As shown, the telescope can reach altitudes as low as 5° above the horizon. However, the telescope cannot point downwards, such that the camera is accessible at ground level; such a capability would significantly increase the size and cost of the mount. To access the camera, a movable platform will be used.

We have carried out a preliminary static and dynamic analysis of the dish structure (Fig. 22). Built from 6 cm diameter steel tubes with 3 mm wall thickness, deformations under gravity of the dish are of order 1 mm. The more critical pointing of the clusters shows a rms variation of 0.24 mrad in both projections for the worst elevation case, before alignment. After alignment at 50° elevation, cluster pointing deviations are reduced to less than 0.15 mrad (rms, projected) for the entire elevation range, and are much smaller for the large elevation corresponding to typical IACT observation modes. The lowest eigenmode of the dish is at 10.1 Hz; values above 4 Hz to 5 Hz are usually considered acceptable for telescopes. Detailed simulations of the behavior under wind and thermal load are not yet available. With typical c_v values around 1.6 in the worst orientation of the dish

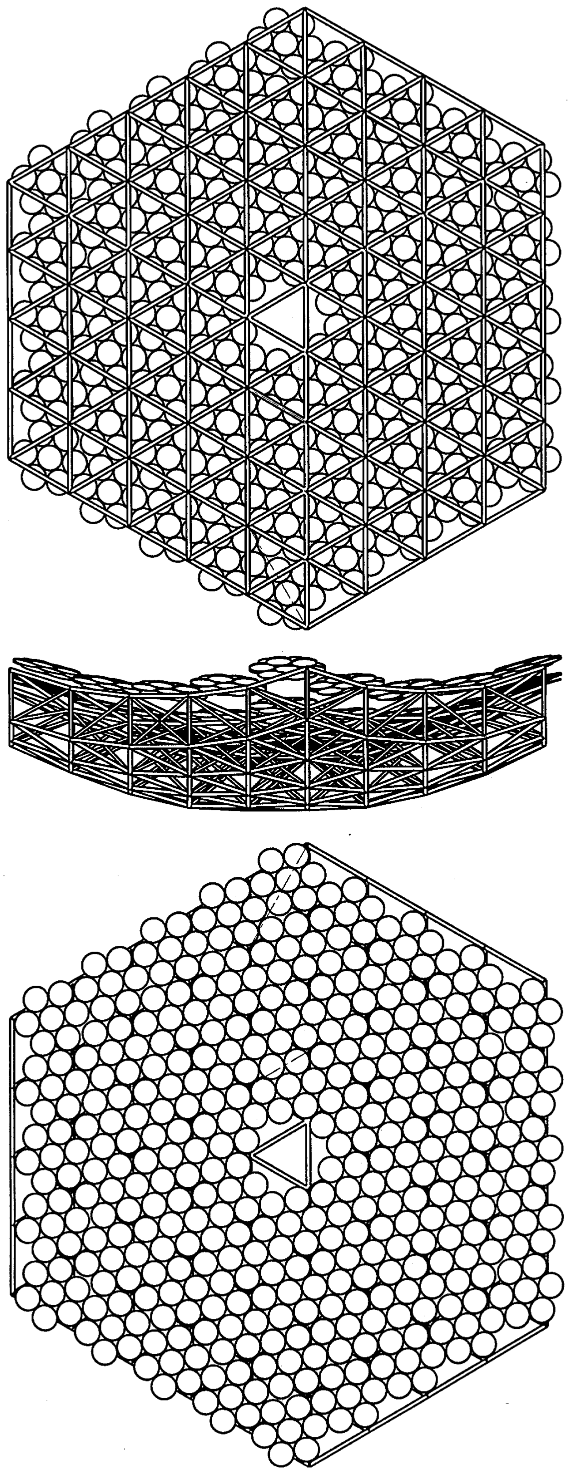

Figure 20: *Mirror and space-frame version of mirror dish; bottom, side, and top view. Groups of 7 mirror tiles are combined into clusters. The support structure is arranged to form triangles underneath each of the 60 clusters.*

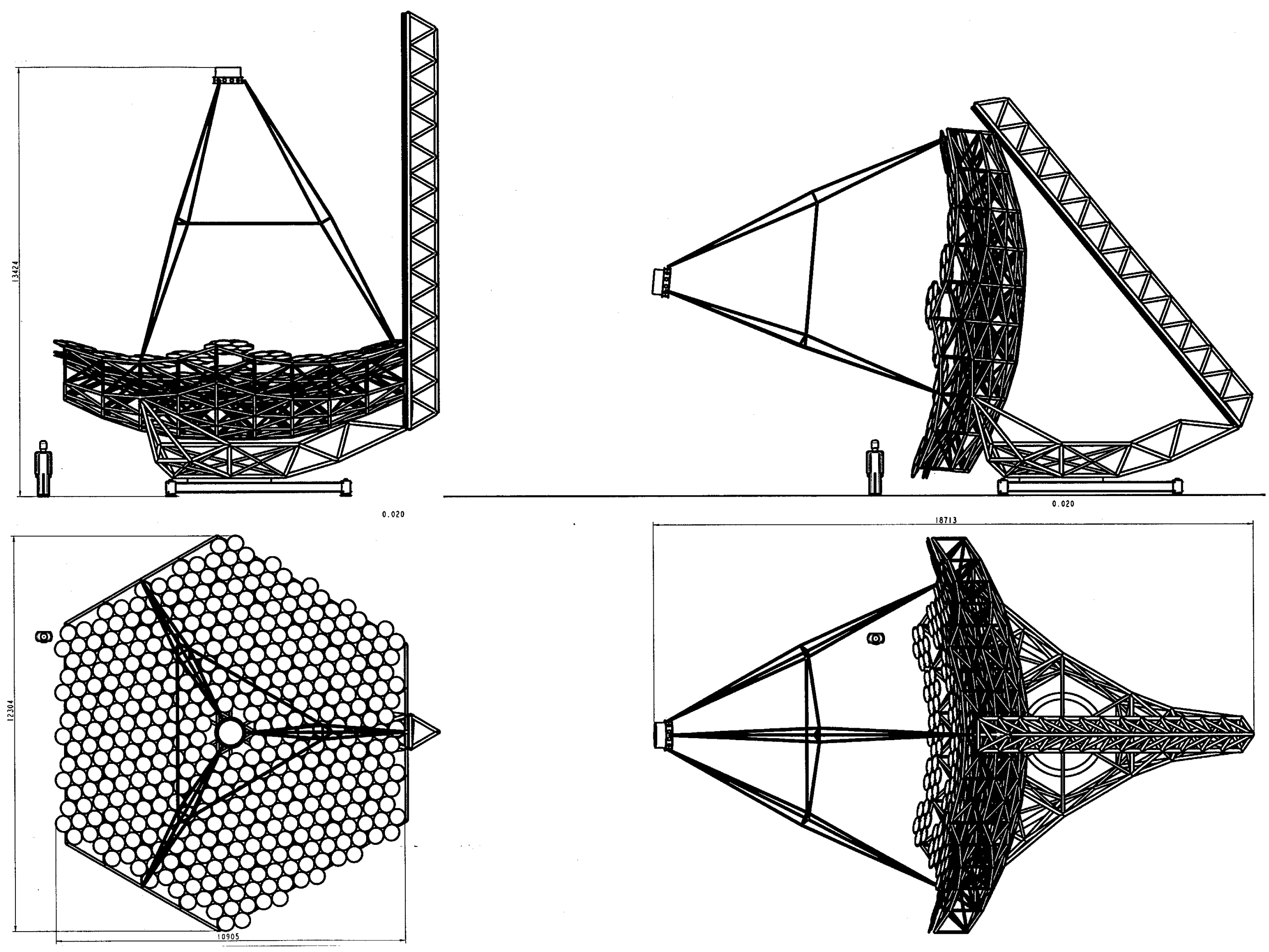

Figure 21: *Side view of a system telescope for the maximal and minimal elevation angles, illustrating the support of dish and camera.*

[4], we find that under operating conditions the wind load is at most 10% of the gravity load, and its influence should be small. At peak wind loads (speeds of 200 km/h), the wind load is about 25 t in the worst orientation, and below 10 t in the survival position. These resulting stresses should still be well within the acceptable range.

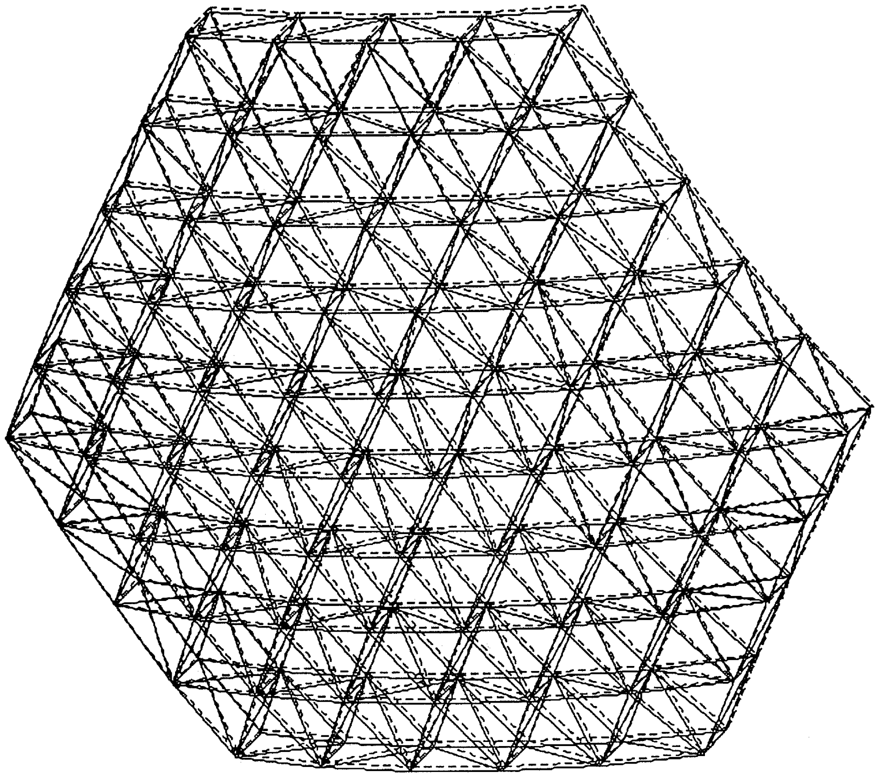

Figure 22: *Simulation of dish deformations under gravity load. The size of deformations is enlarged for the graphical presentation.*

With aluminum masts to support the camera (Fig. 21), the simulations show that fairly large mast diameters - around 10 cm for 2 to 3 mm wall thickness - are required to limit camera deflections to less than 1/2 of the size of a 0.15° pixel. The lowest eigenmodes of such a support are in the range of 3 Hz to 4 Hz. The design can be improved adding diagonal struts or wires (Fig. 23). Then, deflections remain small even for rather thin masts. Another option would be to use carbon fiber masts. Further optimization in terms of stability is required, with the constraint of minimal obscuration of the mirror. Obviously, these calculations represent only a first step and need to be refined and extended in a number of areas, but they demonstrate that the target values for the stability of the dish can be reached with conventional and relatively inexpensive structures.

4.3 Option B: "Communications" Dish with Radial Trusses

Communications antennas in the 10 m to 20 m range have generally converged to mounts with a central, relatively small bearing for the azimuthal motion, and a similarly compact mechanism for elevation [4]; the dish is supported by a set of radial trusses emerging from a central hub (see, e.g., Fig. 24). The design proposed by Vertex is based on this technology, and makes use of off-the-shelf components for the mount. Fig. 25 shows a cross section through the mount and dish, with the azimuthal bearing on top of a support column, the elevation drive with a spindle, and the central cone connecting to the 12 radial trusses. The radial trusses, consisting of 160 mm I beams, are connected by additional beams. Various options have been considered for the arrangement of these secondary trusses. Fig. 26 shows an arrangement where the secondary trusses follow the triangular grid defined by the mirror clusters, providing the support points for the clusters. Unlike for the space frame option, in this design the nodes coincide with cluster centers, implying that clusters are either supported in their center, or from points along the beams rather than from nodes. To minimize shadowing, the four camera masts emerge from the outer radius of the dish, with additional bracing for those four radial trusses. The camera masts are

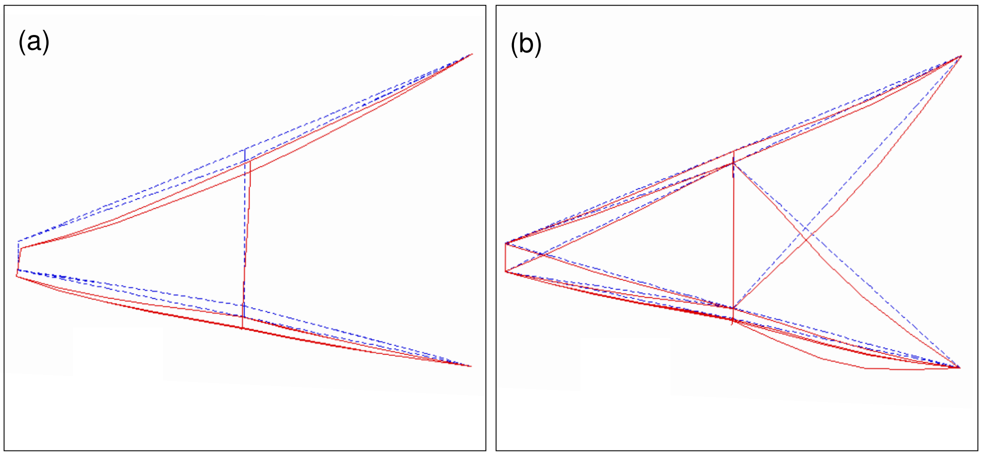

Figure 23: *Simulation of the deformations of the camera masts (relative to the dish support points), for horizontal pointing of the telescope (Side view). The size of deformations is enlarged. (a) Original design, (b) with additional stiffeners.*

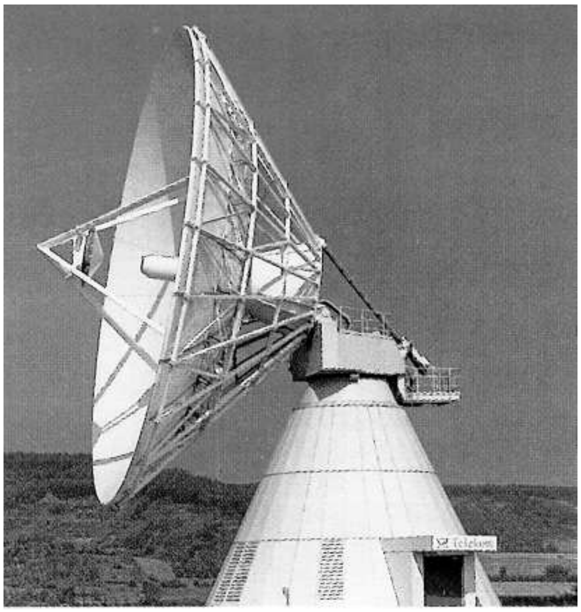

Figure 24: *18.3 m communications antenna with small azimuthal bearing and spindle drive for elevation.*

square carbon fiber tubes, 250 x 150 x 2.5 mm. The total weight of the dish alone, without the mirrors, is slightly below 7 t, and the weight of the support pedestal and azimuth drive is about 16 t.

The dish is driven by two servo-motors in azimuth (the second drive may be used to generate a torque bias, to eliminate play in the gears), providing a speed of $1°/s$ and an acceleration of $0.5°/s^2$; the elevation drive provides typically $0.85°/s$ (varying between $0.7°/s$ and $1.0°/s$, depending on elevation) and $0.5°/s^2$, respectively. The range of motion is 370° in azimuth, and $\approx 0°$ to 90.5° in elevation. Pointing is measured by two 17-bit (0.0028° resolution) shaft encoders directly connected to the axes.

The structural analysis has been carried out for an arrangement of secondary trusses which differs somewhat from the one shown in Fig. 26. This (initial) arrangement (see Fig. 27) had the disadvantage that support points differed between mirror clusters. In their static and dynamic properties, the two versions should be very similar. Table 3 illustrates the stability of the dish, for various load cases, and for light (70 kg/cluster) or heavy (100 kg/cluster) mirrors, and 12 m or 15 m focal length. Of all clusters, 80% have a pointing deviation under load less than the angle shown. A deflection limit of 0.25 mrad is required to maintain a spot diameter of 1 mrad containing 80% of the light (neglecting other mirror imperfections). The deflections of the cluster directions are

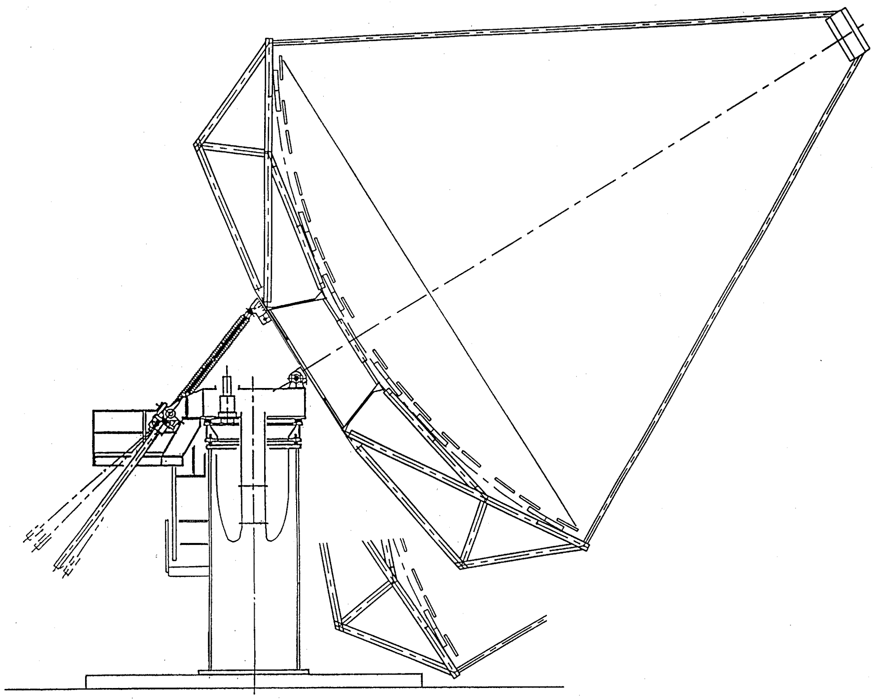

Figure 25: *Cross section through the IACT dish based an communications antennas, showing the azimuthal bearing on top of the support column, the spindle drive for elevation, and the central cone connecting the radial trusses.*

Load	gravity	gravity	gravity	wind 10 m/s	wind 10 m/s
Elevation	0°	90°	0°	0°	90°
Alignment	none	none	at 62°	n.a.	n.a.
Case	80% deflection limit (mrad)				
$M = 70$ kg, $f = 12$ m	0.57	0.21	0.25	0.02	0.03
$M = 100$ kg, $f = 12$ m	0.67	0.25	0.29	0.02	0.03
$M = 70$ kg, $f = 15$ m	0.61	0.22	0.26	0.02	0.03
$M = 100$ kg, $f = 15$ m	0.71	0.25	0.30	0.02	0.03

Table 3: *Deviation of cluster pointing for various load conditions, and different options for the cluster mass M and the focal length f. Of all clusters, 80% have a deviation less than the value given. For best results, clusters are aligned at 62° elevation, resulting in perfect pointing for this elevation, and deviations of equal magnitude for the minimal and maximal elevation.*

given for both the unaligned dish, and for a dish where clusters are aligned at 62.2° elevation. We note that both the cluster mass and the focal length have a rather modest influence on the deflection; from this point of view, there are certainly no strong arguments in requiring a short focal length or light clusters. Concerning their absolute scale, pointing deviations seem large for the unaligned dish, and still somewhat marginal for the aligned dish.

However, the numbers given in Table 3 are only partially relevant, since they refer to deviations from the nominal pointing of the clusters. At low elevations, the dominant mode of deformation of the dish is one where the dish as a whole tilts slightly against the central hub (Fig. 28). As a result, the pointing of the dish is shifted by about 0.6 mrad, but the quality of the image is still good. As discussed earlier, this tilt of dish will be mapped with stars, together with any bending of the camera masts and other global pointing errors, and will be corrected by a corresponding shift of the camera image. A better measure for the quality of the dish is the deviation of the pointing of individual clusters from the net pointing of the dish, defined as the average pointing of all clusters. This revised pointing deviation characterizes the smearing of the image. The relevant numbers

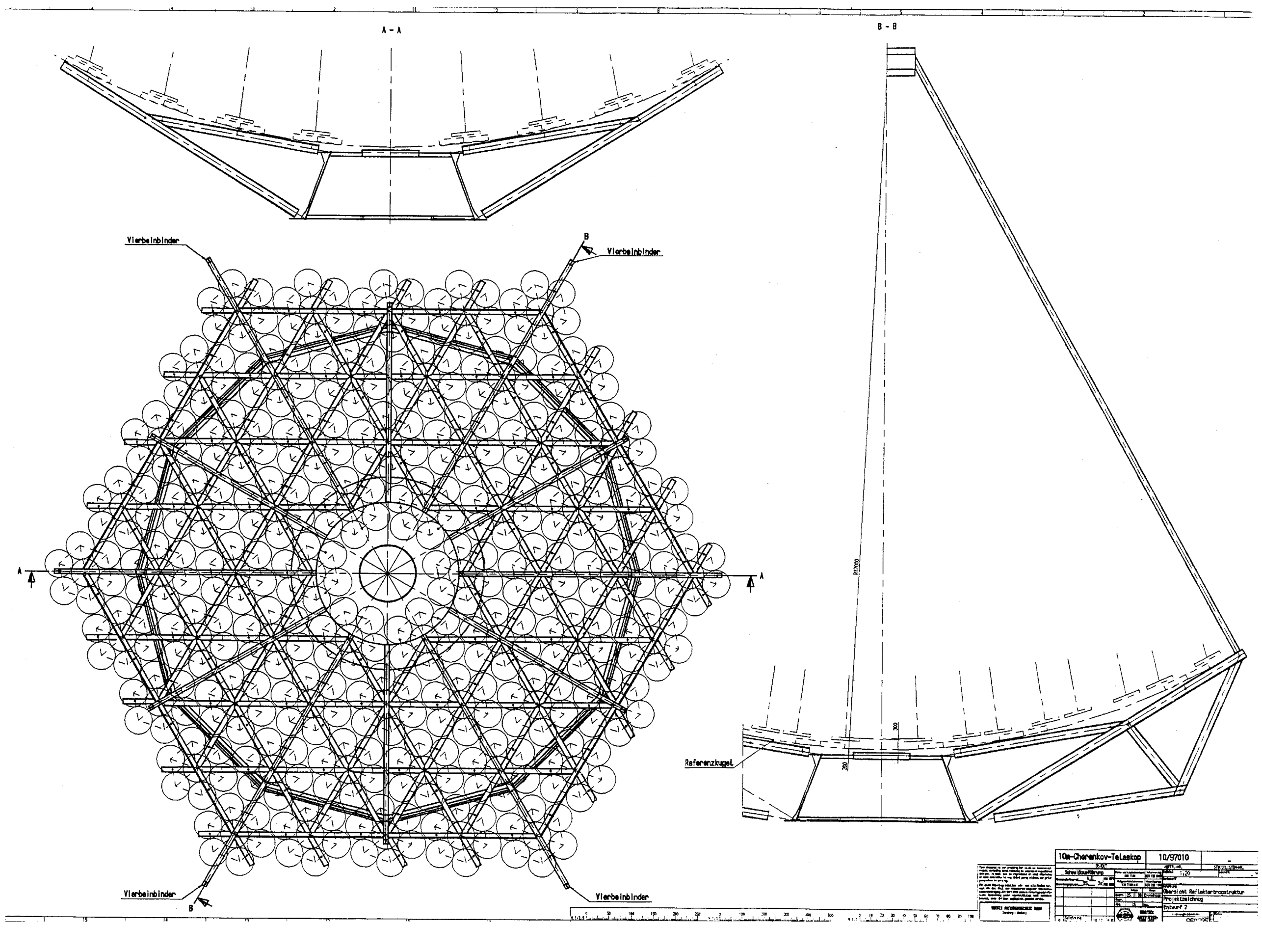

Figure 26: *Truss structure of the dish. The twelve radial primary trusses carry a network of secondary beams at angles of* 0°*,* 60°*, and* 120°*, following the symmetries in the arrangement of mirror clusters. Four of the radial beams extent slightly beyond the dish proper and connect to the camera masts; these trusses have additional reenforcements.*

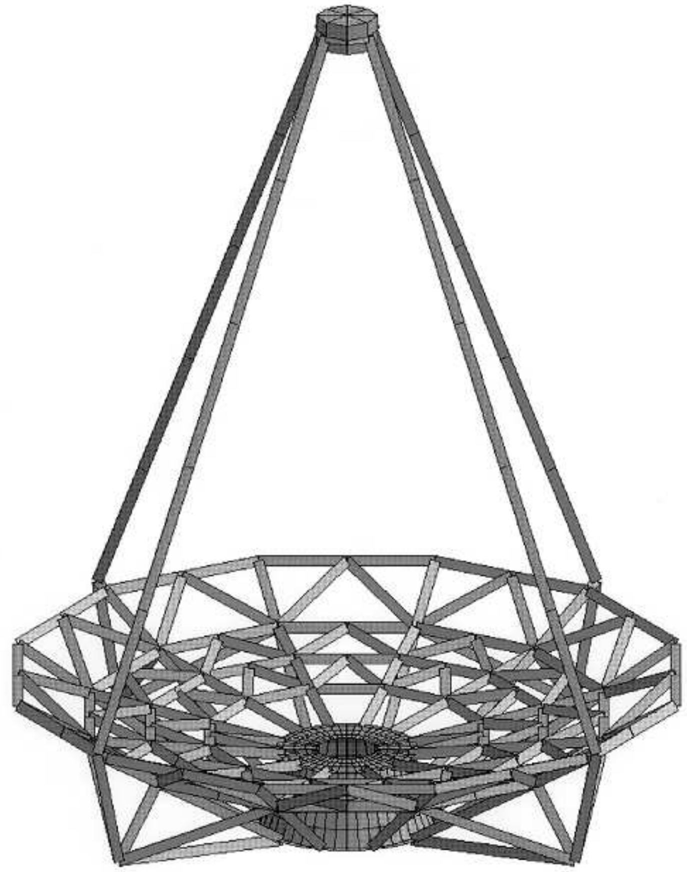

Figure 27: *Initial design of the dish, used in the finite-element analysis of static and dynamic properties.*

	rms x (mrad)	rms y (mrad)	80% defl. limit (mrad)	max. deflection (mrad)
unaligned, relative to nominal pointing	0.65	0.14	0.71	0.95
aligned, relative to nominal pointing	0.28	0.13	0.30	0.77
unaligned, relative to average pointing	0.13	0.14	0.26	0.51
aligned, relative to average pointing	0.13	0.13	0.14	0.54

Table 4: *Deviation of cluster pointing under gravity for 0° elevation, for $M = 100$ kg and $f = 15$ m. Shown is the rms deviation in the x (vertical) and y (horizontal) directions, the limit in the deviation in space for 80% of the clusters, and the maximum deviation is space. The first row shows deviation relative to the nominal pointing for unaliged clusters, the second for clusters aligned at 62°. The next two rows list deviations relative to the average over all clusters. (The distribution of pointing errors is highly non-Gaussian; as a result there is no fixed ratio between rms values and 80% deviation values.)*

are summarized in Tab. 4 for the worst case of a telescope with $f = 15$ m and $M = 100$ kg at low elevation angles; given are the rms deviations in x and y, the 80% deviation in space, an the maximum deviation in space. The numbers show that the dish performs well within specifications. The clusters with large deviations are typically in the center of the dish near the hub, where the dish deforms most (Fig. 28). In future iterations of the design, this region could be enforced. Due to the stiff carbon fiber masts, the sag of the camera (relative to the effective axis of the dish) is only about 0.02°, or about 1/10 of a pixel size.

Table 5 lists the five lowest eigenfrequencies of the system, again for different combinations of focal length and cluster mass. The lowest modes represent oscillations of the camera and the camera masts; with a minimal frequency above 4 Hz for $f = 15$ m, they are in an acceptable range, although the 6 Hz frequencies for $f = 12$ m are more comfortable.

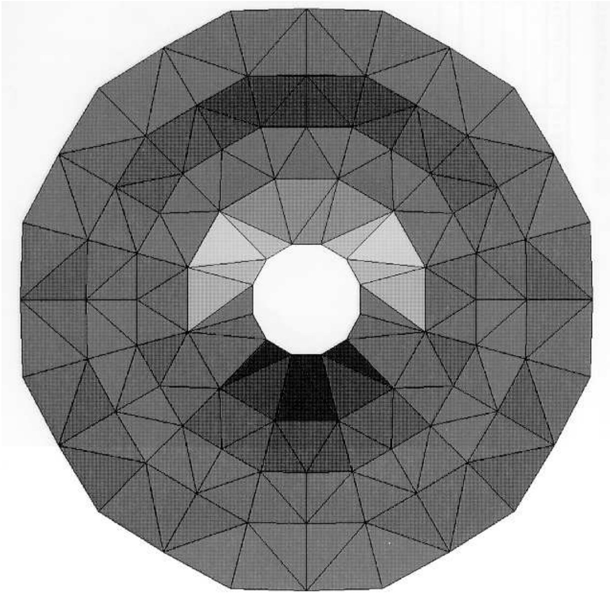

Figure 28: *Example for the pattern of deformations of the mirror dish under gravity, for 0° elevation, and alignment at 62°. The level of shading indicates the angular deviation from the nominal orientation, for planes defined by groups of three adjacent nodes of the truss structure.*

Focal length (m)	12	12	15	15
Cluster mass (kg)	70	100	70	100
Mode	Frequency (Hz)			
1	6.2 (C)	6.1 (C)	4.4 (C)	4.4 (C)
2	6.4 (C)	6.4 (C)	4.5 (C)	4.5 (C)
3	6.6 (C)	6.5 (C)	4.7 (C)	4.7 (C)
4	8.9 (D)	8.5 (D)	6.4 (C)	6.4 (C)
5	9.5 (C)	9.5 (C)	7.5 (D)	7.3 (D)

Table 5: *Lowest eigenmodes of the system of dish and camera for different load cases. 'C' modes involve primarily the camera and the masts, for 'D' modes also the dish participates.*

Analysis of behavior under wind load for operational conditions ($v = 35$ km/h) shows deflections which are small (O(5%)) compared to the deflection under gravitational load. This simply reflects the ratio of the wind load (about 0.8 t worst case for $v = 10$ m/s) to the weight of the dish. Under peak wind loads (200 km/h) and in survival position, the wind load roughly equals the weight the structure.

Given the large number of communications antennas of the 10 m size built and in operation, this dish design represents an extremely conservative and save solution, with costs in a still acceptable range through the use of standard components for the mount. A disadvantage compared to a spherical space frame is that the node points do not exactly match the curvature of the dish, and that additional supports are required (which were included in the structural analysis).

4.4 Mirror Clusters

Fig. 29 illustrates a design for the mechanics of a mirror cluster, based on a lightweight aluminum structure. The individual mirrors are aligned with screws. The cluster as a whole is supported from three points on the mirror dish. Various options have been studied for the adjustment of the cluster. Indicated in the figure is a "hexapod" support, where the cluster is controlled by 6 actuators, allowing a large range of adjustment in all degrees of freedom. Such a support would allow to adjust the distance of the cluster to the focal plane. Since this distance is relatively uncritical, simpler solutions with only two actuator to adjust only the cluster pointing should be sufficient. One option is, e.g., to support clusters in their center using a "Kardan". The actuators

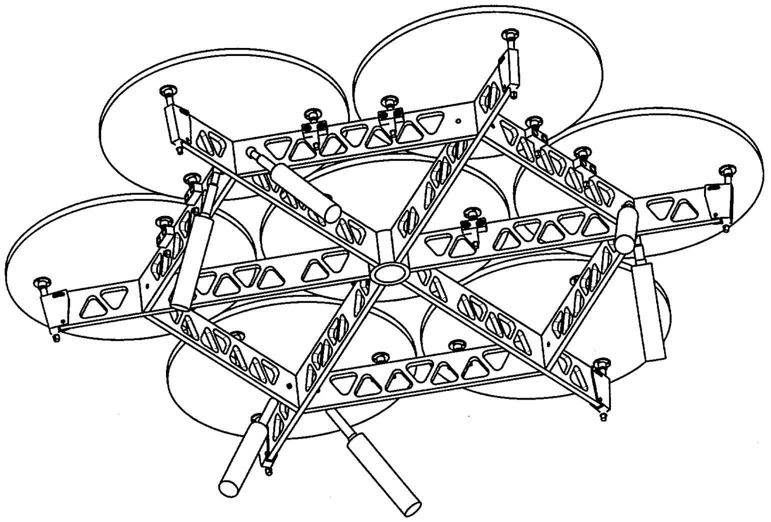

Figure 29: *Example for the mechanics of a mirror cluster.*

will most likely be simple spindles driven either by stepping motors or by DC motors with turn counters; no positional feedback should be required. Extensive prototyping will be required to optimize the performance of the alignment mechanisms and of the stability of the cluster as a whole; first finite element studies indicate that the frame shown in Fig. 29 may be somewhat marginal in its stiffness.

5 Camera

5.1 Field of View, Pixel Size and Pixel Arrangement

In order to allow the investigation of moderately extended sources (up to about 1°) - one of the prime targets of the proposed project - the imaging cameras should provide a field of view of about 4°, in order to allow the unbiased reconstruction of images. For the same reason, we opt for a homogeneous pixel size throughout the field of view. For a good determination of image parameters in the TeV energy range, a pixel diameter of 0.25° represents a good compromise between cost and performance [23]. Smaller pixels, of 0.15° diameter, would improve the angular resolution and the cosmic-ray rejection, in particular in combination with advanced techniques for image analysis [10], which make use of the full intensity distribution of the image rather than using only the first and second moments. At lower energies, showers develop higher up in the atmosphere, and images are smaller; a pixel size of 0.25° in a TeV-IACT is equivalent to 0.18° pixels in a 100 GeV device. In the following, we consider two scenarios: relatively coarse (0.25°) pixels with conventional electronics and small (0.15°) pixels, which would require new developments concerning the readout electronics. Performance estimates used in this Letter of Intent are conservatively based on the large pixels. For a focal length of 12 m, a 0.25° hexagonal pixel corresponds to a size of 52 mm (flat-to-flat); 0.15° imply 31 mm size. For 15 m focal length, the respective pixel sizes are 39 mm and 65 mm. With the larger pixels, we opt for a 271-pixel arrangement, consisting of 9 rings of pixels surrounding a central pixel (Fig. 30, left). A variety of suitable PMTs with 52 mm diameter is available. The larger number of 0.15° pixels is only affordable if in particular the channel cost of the readout electronics can be reduced significantly; this may be possible using custom integrated circuits, as discussed below. As PMTs, one will use 30 mm tubes, which are available at a relatively modest cost due to the large manufacturing volume, compared e.g. to the 19 mm tubes used in the present HEGRA cameras. If the larger 15 m focal length would be realized, 38 mm tubes are a perfect match. The reduced volume and power consumption of an integrated readout optionally allows to install part of the readout electronics in the camera, thereby drastically reducing the number of cables between the camera and the electronics hut. Since the readout is always arranged in groups of 8 or 16 channels, one will in this case assemble the camera out of groups of 8 or 16 pixels (Fig. 30, right), which form a mechanical unit together with their electronics (see below). For repairs, the whole module is swapped. A camera constructed out of such pixel elements will no

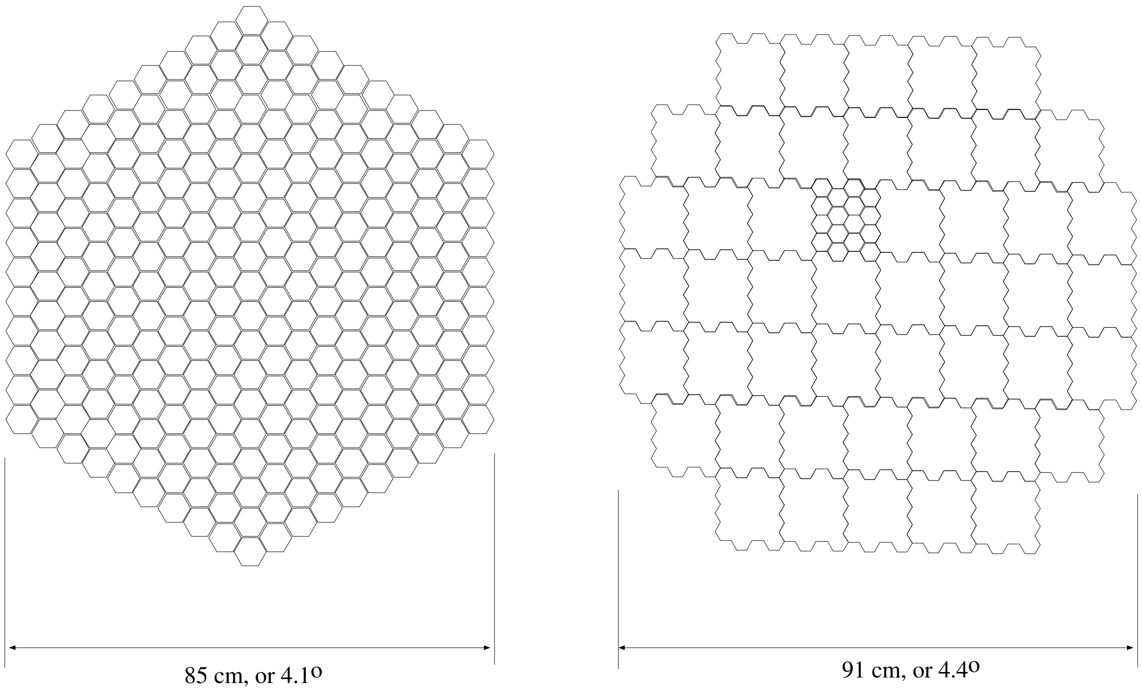

Figure 30: *Arrangement of pixels in the camera. Left: 271 pixels of 0.25° pixel size. Right: 768 pixels of 0.15° pixel size, arranged in units of 16 pixels. Scales are for* $f = 12m$.

longer have a hexagonal field of view, but rather approximate a square with truncated corners; of course, one could add partially filled modules to better approximate a circular shape.

5.2 Camera Mechanics

At least in their most simple incarnation, the cameras of the proposed system are simply scaled-up versions of the present HEGRA cameras (Figs. 31, 32), with a similar construction, and no active elements in the cameras apart from the preamplifiers. The PMT pixels, consisting of the PMTs themselves, the bases, and the preamplifiers, are inserted from the rear side into a matrix made of μ-metal tubes supported by aluminum and Makrolon plates. To improve light collection, an array of light concentrators is mounted in front of the PMT array. To allow a simple measurement of PMT DC currents, the PMTs are operated with HV on their cathodes and anodes on ground potential. For minimal PMT noise, this choice implies that the front part of the pixel support, including the MU metal shields and the light concentrators, are at about the same potential as the PMT cathode, and are insulated from the rest of the camera. A thin UV-transparent plexiglas plate serves as entrance window and protects the pixels from dust and moisture. Cables from each PMT are bundled and plugged with one multipin connector per pixel into distribution boards in the rear of the camera body, where the low voltages for the preamplifiers are distributed and from where the signal and HV cables are routed through the camera masts.

The camera body is made out of aluminum. A thin-walled cylinder is welded to precisely machined front and rear aluminum rings; the outer diameter would increase from 45 cm (for the HEGRA cameras) to about 100 cm, and the length from 40 cm to about 50 cm. The front lid of the camera opens pneumatically, the rear cover can be removed for installation and repairs. Integrated into the rear cover are fans, which provide a steady air flow through the pixel array, and allow to keep operating temperatures below 50° C. For the adjustment of the focal plane, the camera body slides on two rails within a support ring, which in turn connects to the masts. While the light concentrators in front of the pixels already limit the field of view, baffles will be added to eliminate stray light from the ground.

Experience with the 271-pixel HEGRA cameras has been quite positive, and apart from minor modifications, one can essentially scale the design. In fact, a number of issues such as the crowded cabling (Fig. 33) or the need for relatively strong fans are much relaxed due to the larger volume per pixel. In addition, the HEGRA cameras are designed to allow the insertion of a veto scintillator system covering most of the side walls and the back of the camera. This system imposed severe mechanical constraints; it is not needed for system cameras operated

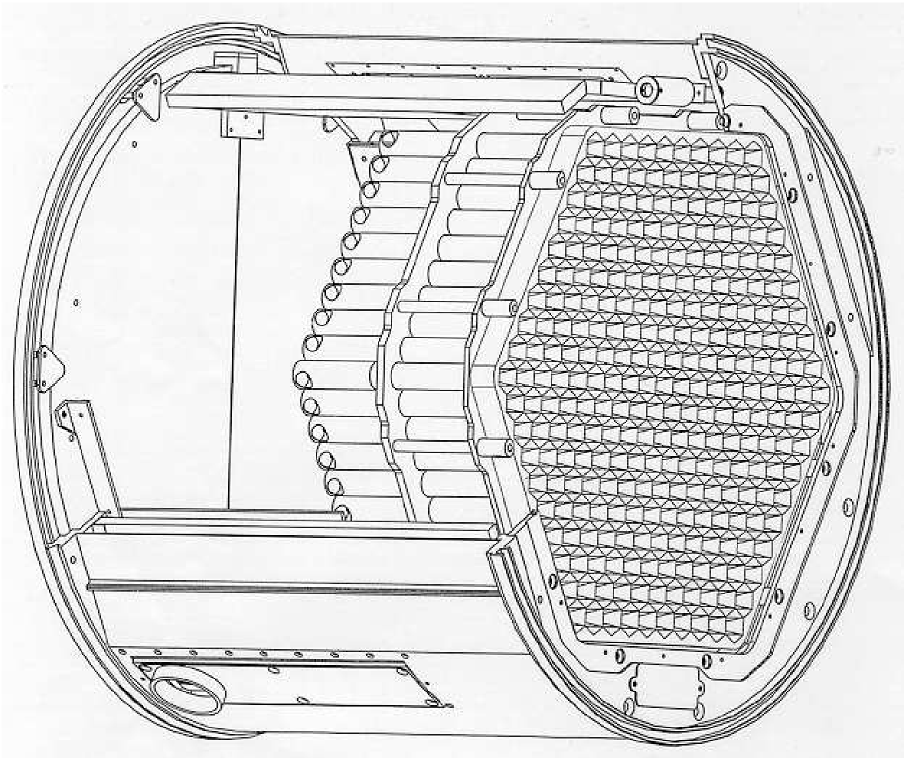

Figure 31: *Mechanical structure of the cameras of the HEGRA IACT system.*

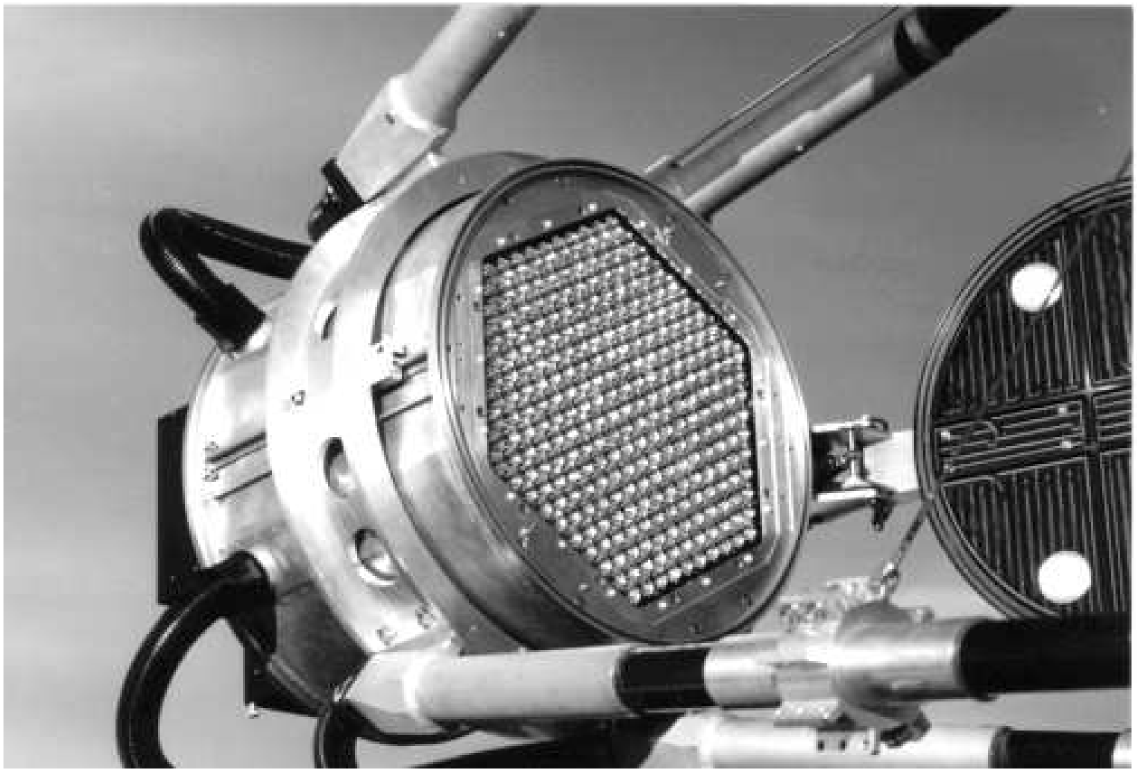

Figure 32: *Front view of one of the HEGRA IACT cameras.*

in coincidence, again simplifying the design. For a camera with integrated readout electronics - relevant mainly

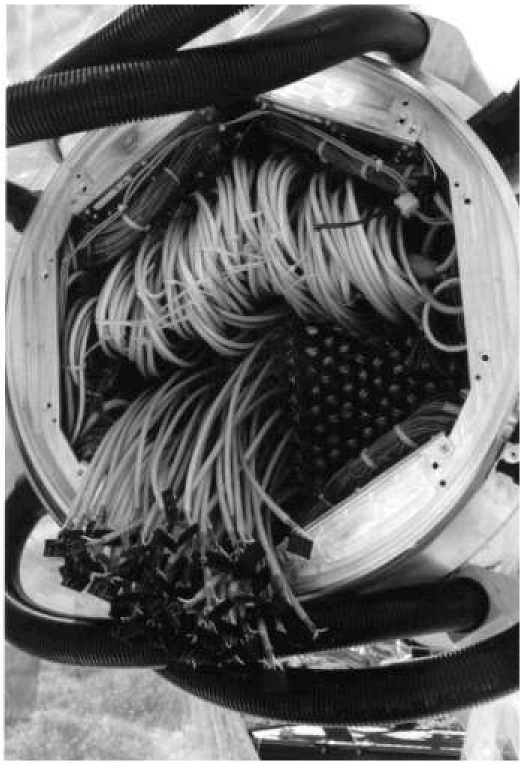

Figure 33: *View into the rear part of a HEGRA 271-pixel camera during the installation of the PMT pixels, showing the routing of cables from the PMTs to the connector boards, which provide power distribution and from where signal cables are routed through the masts.*

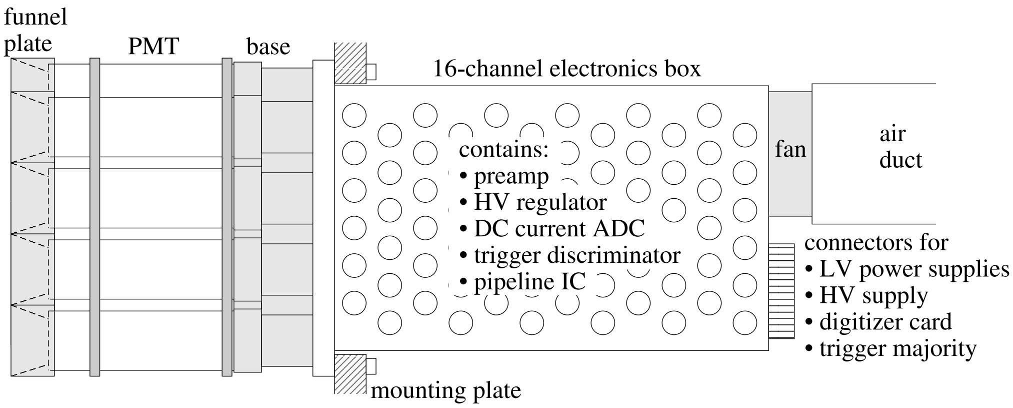

Figure 34: *16-channel PMT module with integrated electronics. The module contains the preamplifiers, discriminators, pipeline ASICs, current monitors, scalers, and HV regulators. It is connected to a trigger decision unit (in the rear of the camera) and to readout digitizers and power supplies (in the electronics hut).*

for the 0.15° pixel option - the layout is changed insofar as now 16-pixel groups rather than individual pixels are the basic units to be inserted into the camera body; such a unit would be about 35 to 40 cm deep, including the PMT, and is connected with multipin connectors to router boards and a trigger board, both in the rear part of the camera (Fig. 34). In this scenario, the camera body would be slightly longer, about 70 to 80 cm.

5.3 PMT and Pixel Assembly

Requirements on the PMT used in the imaging camera include

- High quantum efficiency to about 300 nm, to capture the maximum amount of Cherenkov light. A further extension of the response is not expected to improve the performance of an IACT, since in this range local ozone absorption sets in, resulting in strong fluctuations of the light yield, depending on the shower height.
- Uniform response over the photocathode, and large fraction of usable active area compared to the total front area of the PMT.
- Output pulses with short risetime and length, and small transit time jitter. The relevant scales are set by the duration of the Cherenkov light pulse in individual pixels (about 3 ns rms), the spread of transit times in the mirror (less than 2 ns rms), and the readout sampling frequency (4 to 8 ns).
- Acceptable single-photoelectron response; the requirements are not quite as stringent as for photon-counting applications, but the PMTs should provide a resolved single-photoelectron peak.
- Small rate of large afterpulses. In IACTs with relatively coarse pixels and resulting high pixel trigger thresholds, the pixel trigger rate is governed by the tail towards large amplitudes of the single-photoelectron response, rather than by the coincidental overlap of many photoelectrons [24, 25]. These large pulses occur when the accelerated electron ionizes a residual-gas atom. As a result, significantly higher trigger thresholds are needed than estimated from a Poissonian distribution in the number of photoelectrons. The size of the effect depends on details of the PMT, and its manufacturing process.
- Relatively modest gain of a few 10^4 to 10^5. To limit the anode current and to improve the linearity of the PMT, a low PMT gain combined with electronic amplification is used. Good single-photon response requires that a high gain is maintained at the first dynodes; one may therefore require a PMT with a reduced number of dynodes or read out a dynode rather than the anode.
- Between different PMTs, a limited spread of quantum efficiency and of gain at a given high voltage is required, in order to limit the voltage range covered by the regulators when flat-fielding the camera.
- Finally, one will exclude PMTs with large dark current, which serves more as a general indicator of PMT performance.

One will therefore look for low-cost PMTs with normal window, Bialkali photocathode, 10 or less dynodes with high gain at the first dynodes, and a dynode structure optimized for good linearity and short output pulse length. Appropriate PMTs are available from most major manufactures; candidates include, among others, the Philips 2972, Thorn-EMI 9125 and 9128, and Hamamatsu 3998 30 mm diameter tubes (for $0.15°$ pixels and $f = 12$m), the Philips 2012 and Hamamatsu 580-17 38 mm tubes (for $0.15°$ pixels and $f = 15$m), and the Philips 2262 and Hamamatsu 329 52 mm tubes (for $0.25°$ pixels and $f = 12$m). The final choice of pixel size and camera field of view, and of the PMT type will depend on PMT performance parameters, availability, and cost, and will require about one year of evaluation (see section on schedule).

As for the HEGRA cameras, the PMTs will be subject to a stringent quality control, scanning the homogeneity of the photocathode, and determining the photoefficiency, gain, and sensitivity using the Cherenkov-like spectrum of a Deuterium lamp. Based on the measured sensitivities, PMTs are grouped such as to minimize the spread on HV among PMTs installed in any one camera.

In the single-pixel scenario, the PMT voltage divider and the preamplifer are soldered to the PMT, and the whole assembly is shielded by a thin aluminum pipe. In the scenario with integrated readout, groups of 16 PMTs are connected to a mechanical unit, which also holds the electronic boards (Fig. 34). To provide sufficient board area, one needs to use either multiple boards, or a motherboard with daughterboards for preamps, etc., or a combination thereof. PMT bases are still attached directly to the PMTs. The whole electronics assembly is contained in a shielding cap with ventilation holes; a small fan at the rear end may be required to maintain sufficient air flow.

5.4 High Voltage Supply of the PMTs

To limit gain changes to a few %, the HV applied to the pixels should be stable to better than 2 V; for proper flat-fielding, it should be adjustable for each pixel within a range of a few 100 V. The HV supply of the present HEGRA system will be used as a model. One HV supply per telescope is combined with inexpensive and compact voltage regulators [26] with limited range, providing an adjustable voltage for each pixel. The voltages are set via DACs connected to a simple serial bus, which is in turn driven by a VME I/O register. In the HEGRA telescopes, the regulators are located in the electronics hut; depending on their long-term reliability, we may decide to move them into the cameras, given the larger amount of space available. This would reduce the area and weight of the cable bundles leading to the camera by nearly a factor two [2].

5.5 Alternate Photon Detectors

The performance of an IACT can of course be significantly improved with photon detectors with a higher quantum efficiency than usual PMTs in the relevant spectral range. At this point and in the near future, we do not see a device which provides the appropriate spectral response, large detection area, and low noise (at the level of a single photoelectron) at an acceptable cost. On a longer time scale, avalanche photodiodes may emerge as a serious candidate for a photon detector upgrade. Given the proposed mechanics and electronics for the scenario with off-camera electronics, it will be possible with limited effort to swap the PMTs with their amplifiers against semiconductor devices with appropriate amplifiers, but an otherwise identical readout chain. Even the monitoring feature for DC currents can most likely be maintained, since it does not measure currents directly, but rather uses a current-to-voltage converter in the PMT base to provide a normalized DC offset voltage. In the scenario with front-end electronics integrated into photon detector modules, care should be taken to place detector-specific components such as the preamplifiers on daughterboards, which can be swapped while maintaining the majority of the system.

6 Readout Electronics

6.1 Requirements

The readout system has to digitize the signals from the camera, when the array is triggered, and ideally should also provide timing information. Requirements on the readout include

- Dynamic range: limited at high energies by lack of statistics due to the rapidly falling energy spectrum, Cherenkov telescopes provide a useful dynamic range in energy of about a factor 10 to 30. With pixel trigger thresholds in the range of some 10 photoelectrons, this implies peak signals of a few 100 photoelectrons per pixel. The useful resolution is limited to about 1 photoelectron due to sky noise and the width of the single-photoelectron peak in the photodetectors. As a result, a dynamic range of at least 8 bits or, if possible, 10 bits seems appropriate.

- Charge integration time: the Cherenkov signal from air showers is concentrated within about 3 to 5 ns; PMT output signals for reasonably fast 30 mm to 52 mm PMTs have a similar width. To measure the light yield, the readout system should integrate over this time span. The integration time should not be much longer, since the noise from the night sky background increases with the square root of the integration time.

- Time and pulse shape information: information on pixel timing and pulse shape can be used for various purposes: to reject off-time background light or pick-up noise, to discriminate between hadron-induced and photon-induced showers, and to reconstruct and cross-check the shower direction using the relative timing of multiple cameras. For these applications, one will aim for a timing resolution of about 1 ns, or a pulse-shape recording at about 250 MHz sampling speed.

- Trigger delay: to form a telescope trigger for a single telescope, about 20 to 30 ns are needed, due to by the propagation delays in discriminators, logic gates, and cables. A cell-wide trigger may be late by about 1 μs, depending on the spacing of the telescopes and the orientation of the shower (see trigger section). If telescopes in cells adjacent to a triggered cell are to be read out, delays may exceed 2 μs. During this time, signals must be delayed or stored.

- Readout speed and deadtime: digitization time should not exceed 1 ms in order to allow the readout at rates of a few 10 Hz.

The readout system should also provide a (slow) monitoring of pixel currents and of pixel trigger rates.

6.2 Readout Options

We discuss two options for the readout of the array telescopes

- A flash ADC (FADC) system similar or identical to the one used presently in the HEGRA telescopes, with sampling frequencies between 120 and 150 MHz and 8-bit resolution, and

[2]For safety reasons, shielded HV cables are used.

- A system with custom-designed analog pipeline ASICs, providing sampling rates around 250 to 300 MHz and about 10 bit resolution.

If one omits the option to read out those telescopes which do not have a local trigger, a third lower-performance option could be a system with conventional commercial charge-sensitive ADCs, densely packed on large VME boards.

6.3 Flash ADC Readout System

The FADC readout scheme is summarized in Fig. 35. Amplifiers on the PMT base amplify the AC component of the signal, and convert the low-pass filtered DC current into an offset voltage, for transmission on a single cable to the readout electronics. The AC component of the signal is fed, via a shaping amplifier, to the flash ADC, and also to a pixel discriminator. The shaper attenuates signal components above the Nyquist frequency of the FADC. The ADC [27] is based on an IC containing two 8-bit, 60 MHz FADC circuits; both sample the same input signal and are clocked at 60 MHz with a 180° phase difference, effectively providing a 120 MHz sampling rate. Since both flash ADCs in one chip use the same voltage divider chain, the two data sets can be interleaved after minor corrections. The FADC output is latched and fed into a TTL circular buffer memory, providing storage for 4096 samples, corresponding to 34 μs. A VME motherboard holds shaper daughterboards and FADC hybrids for 16 channels. In one of the HEGRA telescopes, such a 271-channel, 120 MHz system has worked reliably for several months, and has shown a typical amplitude resolution of 1 lsb, and a timing resolution of 1 ns for medium-sized pulses. Due to the recording of the full pulse shape, pulses saturating the dynamic range can be recovered; for such large pulses, the measured pulse area increases like the logarithm of the pulse height, providing a significant increase in the useful dynamic range.

In principle, this readout system can be used as it is for the proposed array telescopes. Taking advantage of the technological developments, one will most likely replace the current 2 x 60 MHz converters and the memory chips by faster circuits, to reach sampling speeds around 200 Mhz. Disadvantages are the modest packaging density - a 271-channel system fills 5 VME crates, including the discriminator cards - the high power consumption - over 3 kW for 271 channels - and the overall channel cost of about DM 500, which would dominate the camera cost. We have therefore developed a conceptual design for an alternative readout, based on custom integrated analog pipeline circuits.

6.4 Analog Pipeline Readout

In this design, the basic element is a switched capacitor pipeline ASIC for storage of the analog signals (Fig. 36). CMOS switches allow to connect small (0.2 to 1 pF) storage capacitors to a write/read line with the analog signal. Using a shift register, one capacitor after the other is connected to the write/read line and samples the signal voltage at a given time. An external buffer amplifier is used to provide sufficient current drive capability. For one or two clock cycles before the write switch is opened, the discharge switch is closed to remove any previous charge from the storage capacitor. With 256 such storage cells and 250 MHz clock frequency, analog signals are stored for 1 μs before they are overwritten. If during that time an array trigger occurs, the clock is removed, and selected cells of the pipeline can be addressed and connected to the write/read line. A switch at the input disconnects in this case the low-impedance write buffer amplifier, and a readout buffer transfers the voltage of the storage cell to an external ADC. For readout, cells will be clocked at lower frequency of 5 to 10 MHz. Several channels are multiplexed into an external 10 to 12-bit ADC, and the digitized values are stored in a FIFO accessible from the global (VME) bus.

Several switched capacitor array ASICs with up to 16384 storage capacitors per chip (128 channels x 128 samples) have been designed and operated at sampling frequencies around 60 MHz [28, 29], and a dynamic range of 2800 has been reported [30]. Devices have - with a free-running shift register - reached sampling speeds up to 300 MHz [31]. The faster digital gates available now in the 0.8 μm CMOS technology allow to overcome this limitation and use clocked shift registers, providing a stable and controlled sampling rate. During the last year, a switched capacitor ASIC chip [32] has been designed and successfully tested by the semiconductor laboratory operated jointly by the University of Heidelberg and the Max-Planck-Institut für Kernphysik, building confidence that the required chip for the telescope readout can be designed and brought to operation on a time scale of about 12 to 18 months. Extrapolating from past experience, the cost per pipeline channel will be less than DM 10/channel.

Depending on the exact configuration of the array and the trigger scheme, the 1 μs storage provided by a 256-capacitor pipeline may be marginal. Pipeline length is limited by the capacitance of the write/read line, and it is not clear if a single pipeline can be extended beyond 256 capacitors. If needed, it is however always possible to split the pipeline into shorter segments, each with its own driver amplifier and output buffer. Similarly, two pipelines can be used in parallel with different input gains to increase the dynamic range.

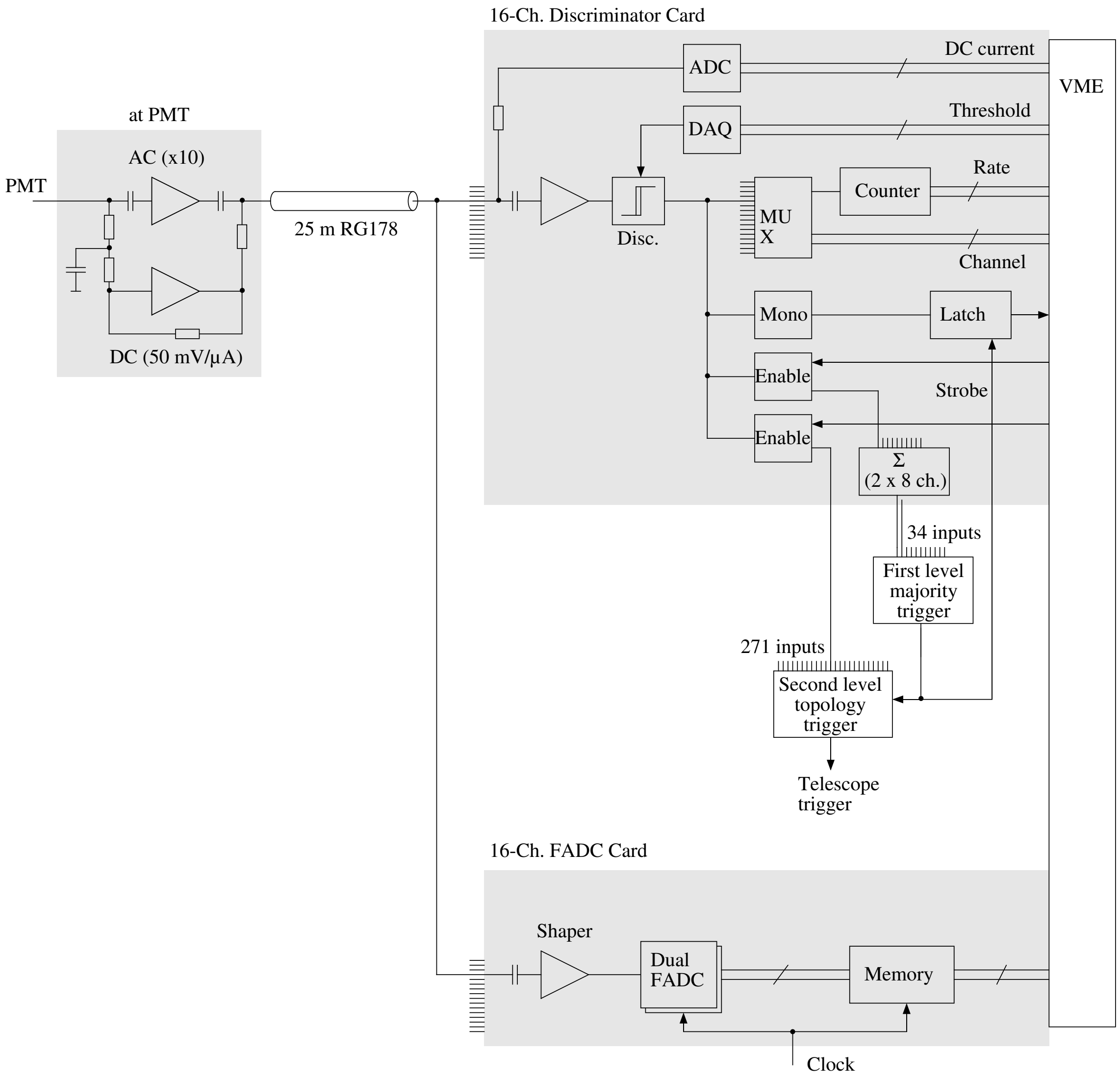

Figure 35: *FADC readout system including preamplifiers, trigger discriminators, and current monitoring.*

The solution with the pipeline chip is pushing technology limits, and involves a certain, albeit limited, risk. The proven flash-ADC system provides a safe backup solution.

6.5 Electronics Installation

With the FADC readout, we feel that the electronics is too bulky and develops too much heat to mount it in the camera; in addition, we prefer to be able to access the components easily. Like presently at HEGRA, VME crates with the FADC modules, the discriminators, the control logic, and the CPU will be housed in a small (2 x 2 x 2 m^3) air-conditioned hut close to the telescope mount.

As mentioned above, the analog pipeline readout might open the way to a much more compact and also more reliable electronics which can be fitted into the camera, thereby avoiding altogether the long signal cables with their weight, bulk, and limited bandwidth. This is particularly relevant for a camera with 0.15° pixels, with its up to 800 channels. With integrated pipelines, the whole readout up to the final multiplexer requires about 25 cm of space behind the pixels. Power consumption is significant - about 1 to 2 W/channel - but seems manageable. In this scenario, only one analog output cable per 8 to 16 channels is required, in addition to the global power and HV connections, and the control bus. Pixels would accordingly be grouped into clusters as mechanical and electrical units; in case of failures, complete pixel clusters rather than individual pixels are swapped. The ADCs, FIFOs, and VME bus interface would remain in an electronics station on or near the telescope mount, together with the electronics for control and monitoring. Whether the advantages of placing part of the readout and trigger system in the camera - improved performance and bandwidth, reduced pick-

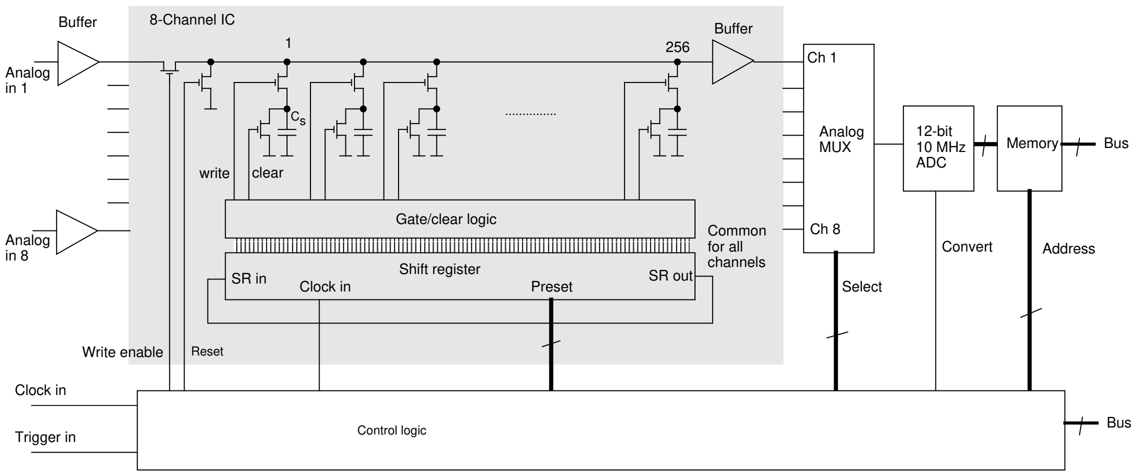

Figure 36: *Switched capacitor pipeline for sampling and storage of the input signal at frequencies between 250 and 300 MHz. See text for details.*

up noise, fewer connections and possibly increased reliability - outweigh the obvious disadvantages - limited accessibility and reduced flexibility - needs further study.

7 Trigger scheme

7.1 Overview

The array trigger is implemented as a multi-level scheme. A first-level camera trigger is generated if the signal in a minimal number of pixels exceeds a preset threshold. The trigger channels are latched and fed into the second-level trigger logic, which imposes additional topological conditions; for two-pixel triggers, the pixels are e.g. required to be neighbors. Such a condition drastically reduces the rate of NSB-induced noise triggers, yet is more than 90% efficient for gamma-ray images [33]. Similar trigger schemes have been proposed for other telescopes [34, 35]. If this second-level trigger fires, the telescope sends a signal to the next higher trigger level, where a coincidence of a minimal number of telescopes within an array cell is required. If this condition is fulfilled, then a reply is sent back to those telescopes which generated triggers, and to additional neighboring telescopes, causing the stop of the sampling clocks, and the readout of the data by their local CPUs. The CPUs accumulate a certain number of events, tagged by their global event numbers, and then send a multi-event data packet to an event builder station. There, the packets are disassembled, data from all telescopes for a given event are collected and formatted, and a record is written to tape and/or disk.

7.2 First Trigger Level - Pixel Coincidence

To derive the local, first level trigger, the output signals of the pixel discriminators are used (see Fig. 35). Pixel thresholds are under remote control; in addition, individual pixels can be taken out of the trigger, either to limit the trigger field of view of the camera, or to exclude noisy pixels. Such noise can be caused by star light, by failures in the pixel or discriminator, or by pickup. A counter can be multiplexed between pixels to monitor the pixel trigger rate. The digital discriminator signals are summed up and discriminated with an adjustable threshold corresponding to the minimal number of pixels required. In the present HEGRA electronics, the length of the discriminator output signals is set to 15 ns; a minimum overlap of two pulses of 3 ns is required to fire the majority discriminator. This first-level trigger signal is generated with a delay of about 40 ns. In a separate branch, the signals of the pixel discriminators are stretched to 80 ns; following a first-level trigger, these signals are latched and are available for readout.

7.3 Second Trigger Level - Image Topology

In case of the coarse-grained (271-pixel) camera, the second level trigger requires that at least two of the trigger pixels are adjacent to each other. The logic uses the discriminator outputs; the implementation is based on gate arrays or programmable logic devices and is straightforward in the sense that these elements provide a sufficient number of gates that one can form an 'or' of all 'and's between adjacent channels [3]. The decision can be taken within less than 50 ns, after which the sampling clock is stopped and a telescope trigger signal is sent out. We have not yet studied the topological trigger conditions appropriate for a camera with smaller (0.15° pixels). In this case, the first level trigger will require three or four pixels in coincidence. At the next level, one might e.g. cut on the number of adjacent pixel pairs.

7.4 Third Trigger Level - Multi-Telescope Coincidence

The implementation of the next trigger level depends on the size of the IACT array. For the initial single, 4-telescope cell, one would follow exactly the scheme used presently in HEGRA and route the telescope trigger signals (over identical cables) to a central station, where they are delayed to compensate for the inclination of the Cherenkov light front, depending on the pointing of the telescopes, and then fed into a majority coincidence, where a minimal number of telescopes is required to trigger the array. The normal trigger mode would require a coincidence of 3 out of the 4 telescopes of a cell. The computer-controlled delays together with the majority coincidence, event counters, and control logic have been implemented on a VME card serving up to 5 telescopes. The relative timing of the trigger signals is recorded by TDCs, both for monitoring purposes and to be able to synchronize the signals from different telescopes. Upon the arrival of an array trigger, the so called event grader master VME card sends a pulse train back to the telescopes, consisting of an initial trigger pulse followed by a preloaded event number. At the telescope, an event grader slave unit receives and decodes the signal, causes the stop of the sampling clock, and an interrupt of the local CPU. Following a central trigger, all telescopes are read out, including those which did not trigger themselves. After the data is read out from the ADCs, the event grader slave is readied for the next trigger.

In a larger array, the array trigger scheme has to be reorganized; instead of a central trigger, each cell of the array triggers independently. This can be implemented either via a trigger station in the center of each cell of IACTs, or, more conveniently, at one of the telescopes. The location in the center allows the smallest propagation delays, but requires an additional enclosure, crate, power supply etc., whereas at a telescope the trigger/delay card can easily fit into an existing readout crate. Which solution is adopted depends somewhat on the readout scheme; with the flash ADC system, memory depth is ample and trigger delay is not a crucial issue. In case of the analog pipeline, the timing budget is much tighter.

Fig. 37 illustrates how the lower right telescope of each cell handles the trigger for that cell; each telescope (except for some telescopes at the periphery of the array) also houses a trigger unit for the corresponding cell of the IACT array. Since each (non-peripheral) telescope is a member of four cells, it sends its trigger signals to four cell trigger units, and receives replies from these four units. In a larger array, one may also wish to read out not only all telescopes of the cell which has triggered, but also the directly neighboring telescopes (Fig. 37). Fig. 38 indicates the delays between the arrival of the Cherenkov light pulse locally at a telescopes, and the arrival time of the global trigger derived from a telescope coincidence; the figure refers to the worst case, namely nearly horizontal showers. The maximum trigger delays are 1.2 μs if only telescopes within a cell are considered and the cell trigger is generated by a station in the center of the cell, 1.6 μs if the trigger station is at the edge of a cell, and 2.5 μ if also telescopes of the neighboring cells are read out (see Fig. 37).

7.5 Trigger Performance and Trigger Rates

A number of sources contribute to the trigger rates of individual telescopes and of the telescope system:

- Genuine cosmic-ray or gamma showers
- Local muons near the telescope
- Particles crossing the camera and causing Cherenkov emission in PMT windows etc.
- Random triggers caused by night-sky background (NSB)

Pixel trigger thresholds and coincidence conditions have to be chosen such that the rate of fake (i.e., non-shower) triggers is a small fraction of the total trigger rate, and that the various trigger levels and the data acquisition system can handle the rate without generating excessive dead time. At the level of 1% deadtime, the hardware and software outlined above sustains rates of about 300 kHz of first-level triggers, 150 kHz of second-level triggers, and at least 10 Hz of third-level triggers; those events are read out and written to tape. Here and in the following, we discuss only the case of cameras with 271 pixels of 0.25° diameters; smaller pixels allow a more efficient rejection of backgrounds at the trigger level and should result in lower background rates.

[3]In the HEGRA system, the topological trigger is presently implemented in software; a hardware unit has been developed by the the University of Kiel and is under test.

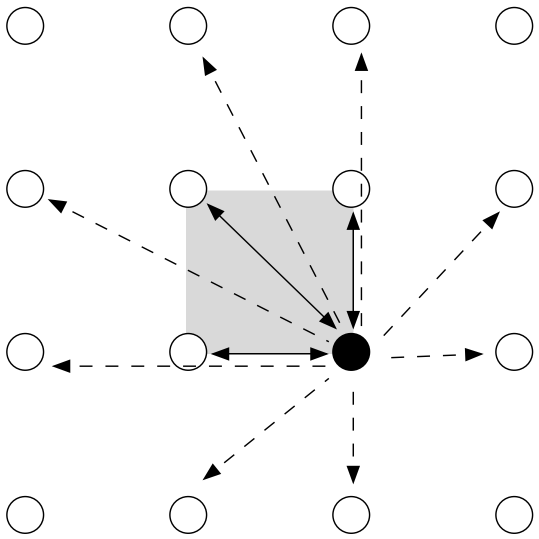

Figure 37: *Trigger configuration for a large array: for a given array cell (grey), the lower right telescope (black) contains the trigger unit, which receives the local trigger signals from the telescopes of this cell (full lines), and returns a cell coincidence trigger to these telescopes. Optionally, one may also trigger and read out the adjacent telescopes (dashed lines).*

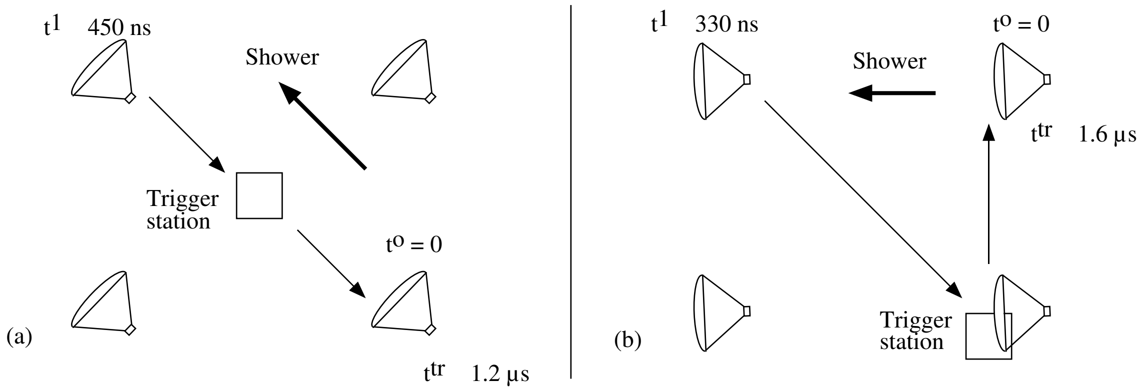

Figure 38: *Illustration of the delays between the local registration of Cherenkov light at a telescope (t_o), and the arrival of the central trigger (t_{tr}), for the worst case of nearly horizontal showers. Indicated is the path with the longest delay, given by the path from the telescope hit last to the trigger station, and from there to the telescope hit first. Spacing of telescopes is 100 m, the signal speed in cables 5 ns/m, and the time to generate a trigger decision is 30 ns. (a) Trigger station in the center of a cell, (b) trigger station at the lower right telescope.*

The trigger rate of genuine showers can be estimated reliably; the final readout rates (which depend on the exact field of view included in the trigger) are indicated in Fig. 39. With cameras with 0.25° pixels and very low pixel trigger thresholds, rates may in some stations exceed 100 Hz, which is likely to result in non-negligible deadtime. At the nominal threshold $q_\circ = 25$ p.e. used for the performance simulations, deadtime is less than a few %. Cameras with small (0.15° pixels) would allow to reduce the cosmic-ray rate by about a factor 4. The load on the first-level and second-level trigger systems due to local muons and direct hits of the camera is uncritical, compared to the peak rates allowed for these systems. Since such fake triggers usually affect only single telescopes, they are almost completely rejected by the inter-telescope coincidence required at the third trigger level.

Random triggers due to NSB represent the most serious limitation. In the relevant spectral range from 300 to 600 ns, the NSB photon flux is $2 \cdot 10^{12}$ photons/m^2 s sr [36] at good optical sites, such as La Palma. As discussed earlier, the rate at which a pixel fires depends on the one hand on the probability that multiple NSB-photoelectrons pile up within the signal pulse width. On the other hand, the long tail of the single-photoelectron

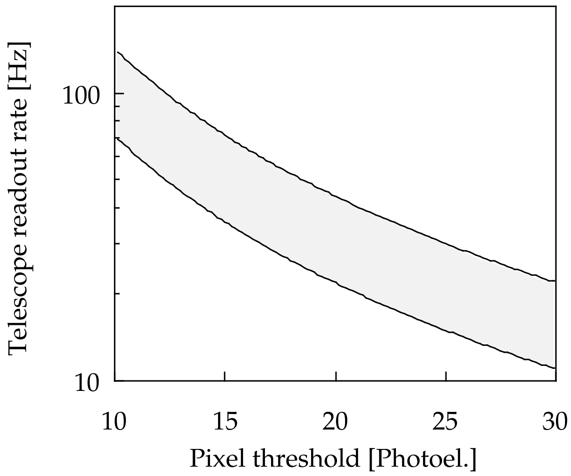

Figure 39: *Readout rate of an IACT in an array operated with a 3/4 cell trigger criterion, as a function of the pixel trigger threshold* $q_\circ$*. Cameras with 0.25° pixel are assumed; the inner 91 pixels are included in the trigger. Rates vary by about a factor 2 between telescopes in the inner region of a larger array, and boundary telescopes or telescopes of a small 4-telescope array. Cameras with smaller* 0.15° *pixels provide improved cosmic ray suppression and hence lower cosmic-ray rates, for a given gamma-ray energy threshold.*

response allows single photoelectrons to trigger with a non-vanishing probability [24, 25]. In the first case, the pixel trigger rate increases with a high power of the photoelectron rate, in the second case, the dependence is linear. The shape of the single-photoelectron response depends on the type and operational characteristics of the PMT; for definiteness, we assume similar characteristics as for the PMTs used in the HEGRA IACTs. Even with the proposed large mirror area, single-photoelectron response fluctuations and not multi-photoelectron overlaps are usually the dominant source of pixel triggers for typical threshold values (provided that a short PMT output pulse of about 5 ns can be maintained). The resulting rates at the various levels are illustrated in Fig. 40. One sees that for thresholds of $q_\circ \approx 10$ p.e. the first-level trigger reaches the 1% deadtime level. At this point, the third-level random coincidence rate is still well below the cosmic rate. The estimates for the system performance given in a later section use a very conservative threshold of 25 photoelectrons; this threshold would even tolerate the pile-up of photoelectrons within a 30 ns integration window, or a 1000-times higher PMT noise rate than assumed here.

8 Data acquisition

8.1 Overview

Purpose of the data acquisition system is to control and monitor the operation of the telescopes, to collect the data packets from the individual telescopes, to assemble them into complete events, to distribute them among processors for monitoring and preprocessing, and to save the data to storage media. Worst-case data rates for individual telescopes - for 100 Hz trigger frequency - are about 250 kB/s, or 1 MB/s for the initial four-telescope system.

The data acquisition system for the proposed array would build upon the experience gained with the HEGRA system, and reuse much of the actual software. As illustrated in Fig. 41, the DAQ system is distributed over multiple levels of processors:

- VME CPUs locally at each telescope for data readout and telescope control
- A VME CPU controlling the global array trigger; for a larger array, this functionality would be integrated into the telescope controllers (see above)
- One or more data servers/event builders for event assembly and data logging
- Processors for quasi-online analysis and quality control
- Workstation(s) to control the system, and to display events and control information.

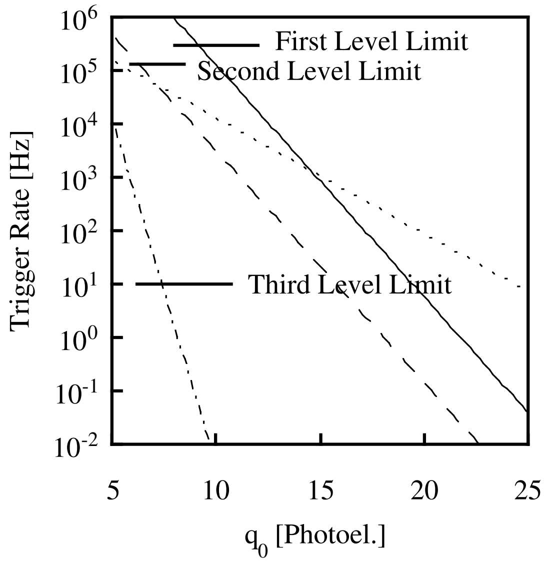

Figure 40: *Expected NSB random trigger rates of individual pixels (dotted line), of the first level camera trigger (2-pixel coincidence, full line) of the second-level camera trigger (neighbor condition, dashed line), and for a coincidence of 3 out of 4 telescopes (dashed-dotted line), as a function of the pixel trigger threshold $q_\circ$. The resolution time is 15 ns for the pixel coincidence, and 100 ns for the telescope coincidence. 217 out of 271 pixels of size* 0.25° *are included in the trigger. Also indicated are the peak rates allowed for 1% deadtime.*

The various processes communicate using a UDP-based protocol (for fast data transfer) or using higher-level protocols (for less time-critical tasks) via local networks.

The HEGRA system software was designed to provide a simple and efficient user interface, guiding the user through the required operations and providing built-in help features. A key feature of the experiment is that almost all hardware parameters such as voltage settings, trigger conditions and thresholds etc. are under computer control. Standard configurations are initialized through configuration files, and can be changed only through interfaces which record all actions in history files, allowing later to reconstruct the status of the system at any given time, and reducing the chance for user errors.

For use with the proposed array, the present HEGRA software needs only modest upgrades; we consider e.g. the use of a history and configuration data base to replace the present file-based approach. On the hardware side, the normal evolution of processors and networks over the few years between the commissioning of the HEGRA system and the installation of the proposed array provides sufficient performance gain to handle the increased rates and data volumes. Most likely, one will continue to use VME CPUs under LynxOS for the readout and control of the telescopes, based on fast PowerPC processors like the 604e (or its successors) instead of the present 68040 CPUs. Pentium Pro or PowerPC based PCs (possibly in a multi-processor configuration) under Linux could serve for event assembly, data handling, and monitoring. In order to cope with the higher trigger rates, the present Ethernet connections to the telescopes will be replaced by a higher-speed network such as Fast Ethernet.

In the following, we give a brief overview of the functionality of the various DAQ components.

8.2 Front End Processors

The DAQ software running in the front-end processors at the telescopes uses multiple threads for the readout of the hardware into a software ring buffer, for the preprocessing and packaging of data and the transmission from the ring buffer to the event builder station, for the communication with the user, for the tracking of the telescope, and for the control and monitoring of the telescope hardware. Care is taken to synchronize processor clocks (used to determine telescope orientation) throughout the array. The present HEGRA system allows to read out 271-pixel cameras at rate of about 10 Hz, at 2% to 3% deadtime of the system, governed mainly by the readout and buffering of data in the front-end processors. At higher trigger rates, limitations of the network bandwidth and the (single) event builder CPU become relevant. With modern CPUs, a reduction of the front-end readout time to about 1 ms is expected. The third-level rate limits used in the previous section are based on this performance. If required, one has the option to reduce the readout time further by using multiple

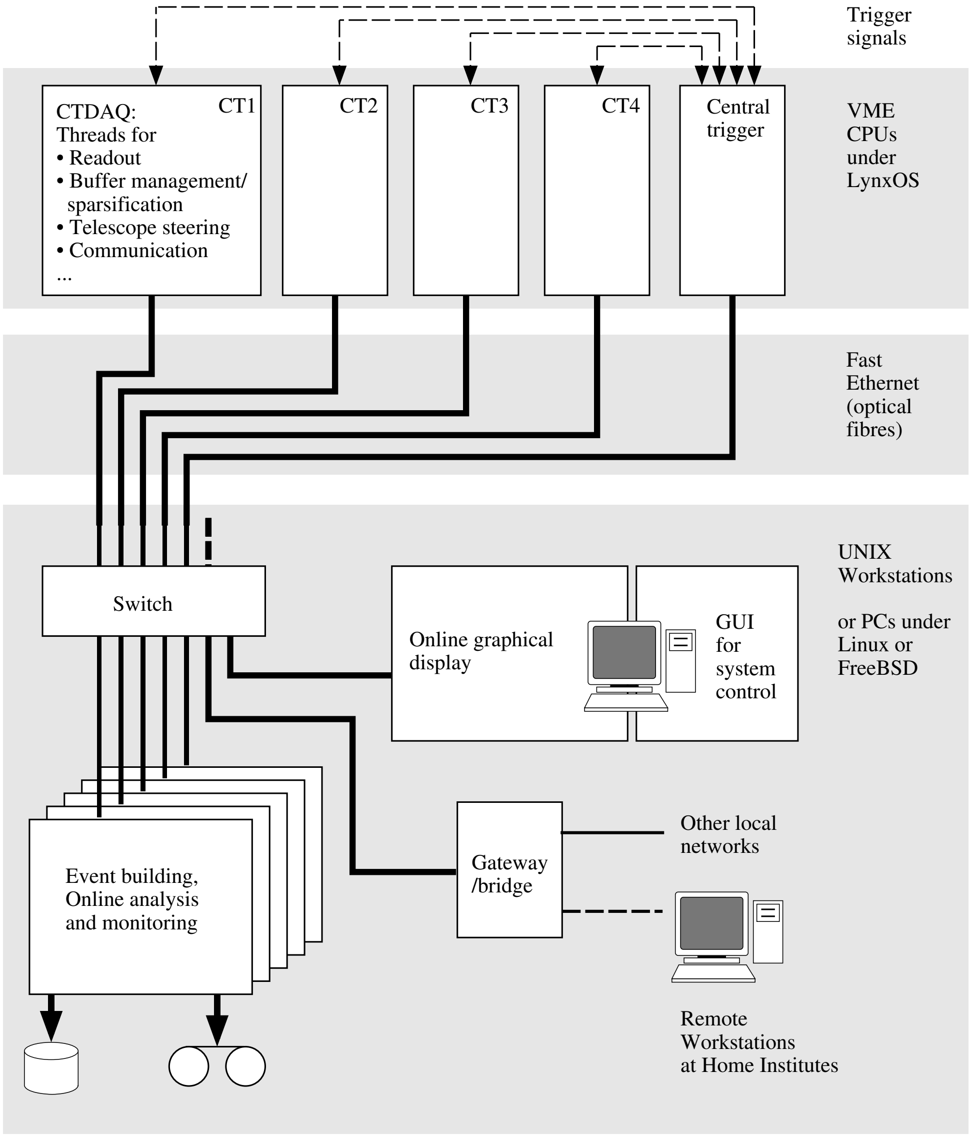

Figure 41: *Architecture of the data acquisition system*

CPUs; presently, five VME crates are read out by a single CPU. Given the cost of VME interconnects and the decreasing cost of high-performance VME CPUs, the cost increment is only about 4 KDM per additional CPU.

8.3 Central Trigger Station

The software running in the central trigger station(s) is based on the same tools and schemes as used in the front-end processors. After an array trigger, the CPU reads out the TDCs etc. located at the trigger station, and sends - just like the telescopes - an event message to the event builder, containing the local data, as well as the time, event number etc. After handling the interrupt, the event number for the next event is loaded into the event grader master, to be distributed with the next trigger signal. In addition, the central trigger CPU(s) keep(s) track of various monitoring quantities. The functions of the central trigger processor could also be handled by one of the telescope CPUs in addition to the telescope readout; in a large array, this solution is preferred.

8.4 Networking

In the present HEGRA system, data is collected from the front ends using Ethernet; all telescopes and the central station are connected to the one single network. The transmission protocol is optimized to avoid collisions on the network. For the proposed system, network bandwidth needs to be increased by at least a factor 10 for a four-telescope array, and more for the full array. This increase can safely be realized by two measures:

- Use of high-bandwidth network components; currently, Fast Ethernet would be the preferred solution, providing a factor 10 increase in raw bandwidth.
- Distribution of the load among several network segments, e.g. by using multiple event builder processors and a fast (commercial) switch to route data between telescopes and event builders.

The required data rates are modest by modern standards, and a variety of commercial solutions are available.

8.5 Data Server, Event Builder, Processor Farm

The event builder unit(s) receive(s) the multi-event packets from the telescopes and the trigger station(s), sorts them according to event numbers and stores them in buffers until an event is complete, i.e., all relevant telescopes have sent their data. Complete events are then written to disk, and later copied to tape. Upon request, events or parts thereof can be sent to user or control processes for online display or monitoring. At present, this distribution of events supports only a limited rate; to allow online reconstruction of the full data, a faster mechanism needs to be implemented. One efficient solution is to use a shared memory region in a multiprocessor machine. For a larger array, event building will be split up among several machines. Even for a four-telescope array, with its relatively modest worst-case data rate of 1 MB/s, this may be a convenient solution. For online data reduction, a small farm of processors will be installed; rather than having separate processors for event building and analysis, the front-end processors could send their data directly to the farm nodes, distributing the load. The address of the target processor would then be distributed with the event grader units, along with the event number.

8.6 Control and Monitoring Software

All telescopes are controlled, either individually or as a system, from a central station using a graphical user interface. We expect the user interface to evolve from the interface developed for the HEGRA IACT system. This interface is based on the Tk/Tcl package. Fig. 42 shows the main control screen. The "main" menu is used to control the system as a whole via buttons. The actions caused by clicking a button can be very complex, consisting of processes based on C-code, Unix shell scripts, remote logins on other processors, and command/data transfers via UDP. The menus adapt the disabled/enabled status of all buttons automatically, inhibiting disallowed command chains, and provide online help. A second row of buttons control the online display, which can show

- the individual telescope images, optionally indicating the trigger pixels and the image parameters
- the pixel rates
- the pixel currents
- a graphical representation of the 3-D shower reconstruction based on the image parameters

or combinations thereof. In addition, trigger rates and random coincidence rates may be indicated, and color-coded status fields alert the user in case the slow control systems indicate a malfunction of a telescope.

9 Auxiliary Systems, Calibration, and Monitoring

Apart from the components described above, an array telescope will need a variety of additional systems to be fully functional and reliable. These include, among others

- Encoders to monitor the tracking of the telescope, and software to control the tracking
- A precise clock for event timing at the μs level
- TV cameras and optical sensors to monitor telescope tracking, bending of the camera masts, deformations of the mirror dish, and adjustment of the mirrors
- A laser calibration system for flat fielding of the camera
- An optical "test pulse" system to monitor telescope sensitivity
- A system monitoring weather conditions.

In the following, we will briefly address these components.

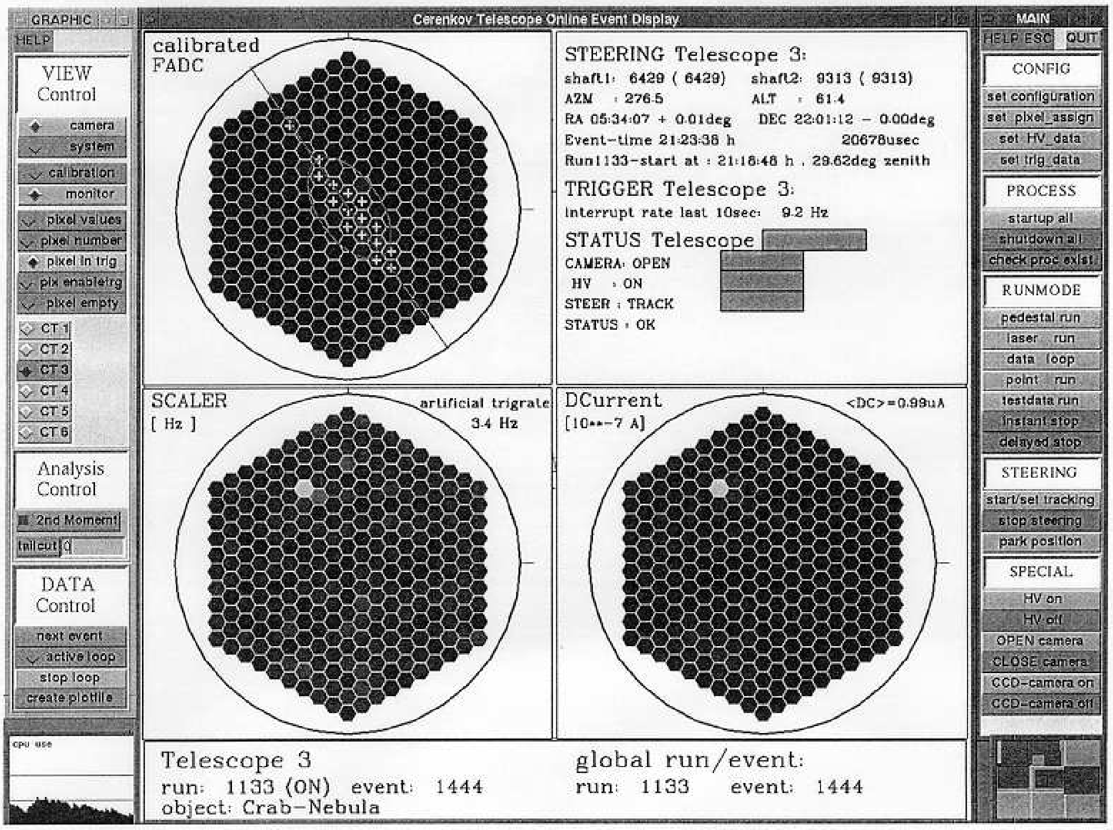

Figure 42: *User interface for the HEGRA telescope system, showing (from left to right) the control panel for the event display, the online event display, and the panel for telescope control.*

9.1 Telescope Tracking

The pointing of the telescopes is measured using commercial encoders connected to the two axes; 14-bit encoding is required, and higher resolution (16 bit) would be preferred. Based on the experience with the HEGRA system, is seems advisable to provide redundancy in the monitoring of the pointing; this could be achieved either by a second set of mechanical encoders, or by alternate devices such as inclination sensors. The information from the encoders is used to drive the telescope stepper motors via commercial VME controllers. In the tracking mode, deviations between the nominal and the measured position are used to correct the stepper frequency, with appropriate damping terms to avoid sudden accelerations [37]. In the HEGRA telescopes, deviations from the nominal pointing do not exceed one lsb of the encoder under normal conditions. For fast positioning, the telescope moves at constant velocity and the feedback loop is only activated once the target position is approached. For the system telescopes, we aim for fast positioning within 3 min. for the maximum travel distance.

9.2 Monitoring of Telescope Tracking using Stars viewed in the Camera

The stereoscopic reconstruction of air showers is very sensitive to deviations from the exact pointing of the telescopes. So-called "point runs" will be used to calibrate pointing deviations. In these runs, the image of a star is scanned in fine lines across one or more pixels, and the DC current is measured. For a given position of the image, the current is proportional to the point spread function of the mirror, integrated over the pixel area. From such scans, both the location of the image - and hence pointing deviations - as well as the width of the point spread function can be determined. This technique has been applied successfully for the HEGRA telescopes. Fig. 43 illustrates the differences between the nominal positions of stars, and their observed images, as a function of altitude and azimuth. In some areas, deviations exceed 0.2°. The data are then fitted with a model including atmospheric refraction and, as free parameters,

- the bending of the camera masts (assumed to be proportional to sin(*elevation*))

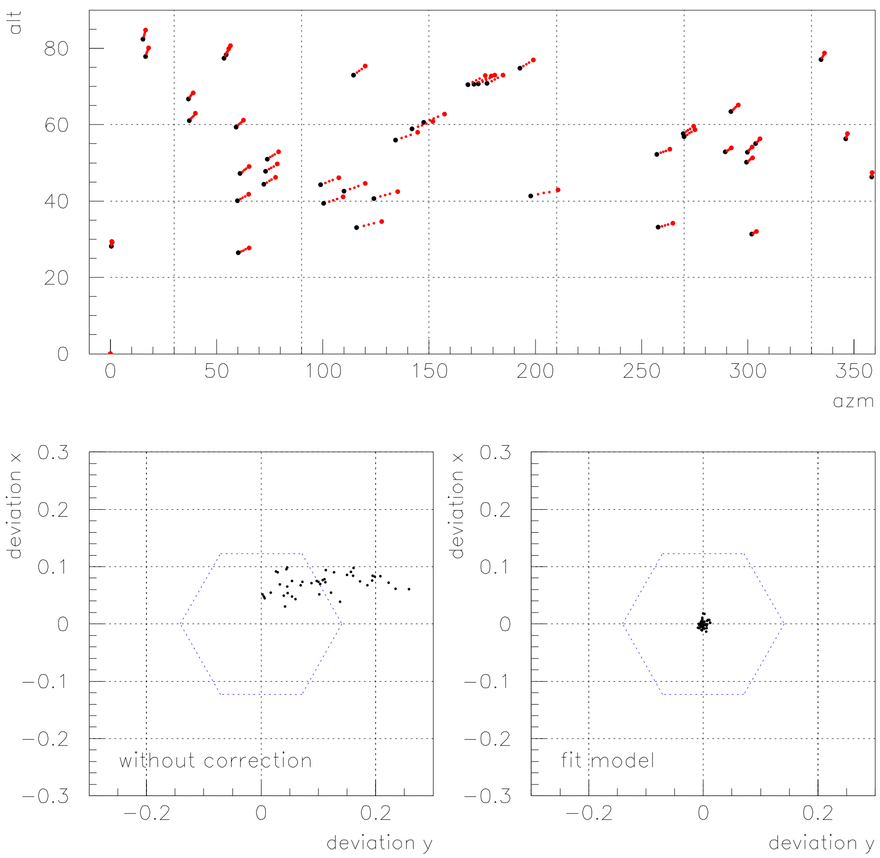

Figure 43: *Top: pointing deviations of one of the HEGRA telescopes as as a function of azimuth and altitude, determined using images of bright stars. The (enlarged) deviations are indicated as vectors. Bottom left: measured deviations from the nominal pointing for an ensemble of stars. For comparison, the outline of a 0.25° camera pixel is superimposed. Bottom right: deviations after correction using the model discussed in the text.*

- an offset of the camera from the optical axis of the telescope
- a deviation of the azimuth axis from vertical alignment
- an offset in the shaft encoder values measuring azimuth and altitude
- a modulation of the azimuth shaft encoder, e.g. due to eccentricity of the axes or gears.

This model provides a consistent description of the data; after a corresponding correction, all star images appear at their nominal positions, with an rms deviation of less than 0.005°, sufficiently precise for the most ambitious reconstruction techniques.

9.3 Monitoring of Telescope Geometry and Tracking with TV Cameras

We foresee at least three CCD cameras to be used for additional monitoring of the tracking and the telescope geometry:

- A camera near the center of the telescope, viewing a region of the sky of about 5° by 5°. Stars viewed by this camera are used to check the pointing of the telescope. Ordinary TV cameras show stars up to *mag* 6. To (almost) always have stars visible within the field of view, an astronomical camera with reduced noise and larger integration time should be used.

- A camera in the center of the telescope, viewing (pulsed) LEDs surrounding the image plane of the camera, in order to monitor bending of the telescope masts. A normal TV camera is sufficient.
- A camera near the periphery of the telescope dish, to monitor deformations by comparing the image with that of the camera close to the center of the dish. A normal TV camera is sufficient, since continuous monitoring should not be needed.

The frames from these cameras are digitized (using e.g. VME frame grabbers) at a low rate, and the position of detected light sources is determined online and is written into the monitoring data stream. Given the limited number of stars in the field of view of the sky cameras, the automatic identification of object should be straight forward, and an alert will be given in case of significant pointing errors.

9.4 Laser Calibration System

Like in the HEGRA telescopes, a laser calibration system will be installed for flat-fielding of the camera and for quick checks on the conversion factor relating the ADC count to the number of photoelectrons seen by a PMT. A low-power commercial Nitrogen laser with a pulse length of about 0.8 ns and a peak repetition rate of a few Hz is used to illuminate a small scintillator at the center of the mirror dish. The scintillator is chosen to provide a spectrum resembling the spectrum of Cherenkov light; the angular spread of the light is large enough to illuminate the camera uniformly to very high precision. Laser data are used both for the initial adjustment of PMT high voltages, and for the continuous (several times per night) calibration of the PMTs; interleaved with data runs are short laser calibration runs. The width of the distribution of pulse heights measured in a pixel is dominated by photoelectron statistics and can be used to determine the average number of photoelectrons in the laser signal, and hence the conversion factor, up to a correction due to the width of the single-photoelectron response of the PMT [4].

9.5 Absolute Calibration Techniques

The absolute calibration of an IACT, i.e. the determination of the factor relating the ADC pulse height to the number of photons incident on the mirror, is a continuing theme in the analysis of IACT data, in particular concerning flux determinations. A number of methods are in use, such as

- Detection of muon Cherenkov rings [38, 39]. This technique measures all relevant factors, including effective mirror area, mirror reflectivity, efficiency of light collectors, PMT quantum efficiency etc.. Drawbacks are the usually limited statistics of muon rings, the need to use Monte Carlo simulations to predict expected ring intensities with their dependence on muon impact parameters, and finally the slight difference in the Cherenkov spectrum of nearby muons, which has a larger UV contribution than the light from showers high up in the atmosphere.
- Comparison of measured and predicted cosmic-ray detection rates (see e.g. [40]). This calibration scheme summarizes all relevant factors, even including light attenuation in the atmosphere (up to small corrections due to the different longitudinal development of hadron and photon showers). It is limited by uncertainties concerning the simulation of hadronic cascades, and, more importantly, by the imperfect knowledge of the cosmic-ray elemental composition.
- Monitoring of the intensity of stars with spectral characteristics similar to the Cherenkov spectrum [41], and comparison with photometrical data. This scheme again includes all factors; a problem is that this technique relates DC pixel currents to photon flux, rather than AC pulse height. Required is a certain amount of observation time under photometric conditions to allow to average over a large enough sample of objects and observations.
- Determination of the ADC count corresponding to a single photoelectron, either by direct observation (usually with additional gain in the signal chain) or indirectly using e.g. the width of the laser peak. This technique has practical problems - in either case, one needs to know the shape of the single-photon response down to very small pulse heights in order to average over this distribution, or to calculate its width. Another difficulty is that it measures one contribution to the overall calibration; values for quantum efficiencies and reflectivities have to be assumed, and are not tested.

[4] Fluctuations in the laser output itself have of course to be removed, either by normalizing to a reference PMT viewing part of the direct laser pulse, or using the average response of all pixels of the camera.

- Cross calibration of the telescope system with another calibrated photon detector, using a distant (pulsed, monochromatic) light source illuminating both detectors. This method again accounts for all effects apart from atmospheric absorption, and allows to check the detection efficiency as a function of wavelength. A pulsed laser with a wavelength-shifting scintillator and band-pass filters provides a suitable light source. The difficulty is that a Cherenkov telescope is about the most sensitive detector for pulsed optical radiation; a calibrated photo diode with low noise electronics and signal averaging is 10000 times less sensitive. A cross calibration requires the use of a calibrated attenuator to provide different pulse intensities of known ratio. The control of systematics is nontrivial.

To obtain a reliable calibration, many or all of these methods need to be explored and combined. For the most part, they do not require additional hardware which is permanently installed at the telescopes. For the measurements with the distant pulsed laser, a spare calibration laser can be used and moved from telescope to telescope. The detection rate for muon rings can be enhanced by lowering the pixel trigger thresholds of the telescopes and raising the number of pixels required in the coincidence; this can be achieved completely by computer control using a modified setup file.

9.6 Monitoring of Environmental Conditions

In the analysis of IACT data, runs with poor weather conditions have to be rejected. In order to provide objective criteria, some recording of the relevant conditions is required; this serves also to alert the shift crew in case of changing conditions. In addition to general meteorological data, we found it useful [42] to monitor the sky brightness in a window roughly equivalent to the IACT field of view, for different wavelength regions. A global monitoring is of course provided by the average PMT DC current; however, the spectral resolution (in about 4 to 5 bands) provides increased sensitivity. Beginning overcast e.g. causes characteristic fluctuations in the ratio of intensities at different wavelengths. The experimental equipment is simple - a PMT equipped with a filter wheel and simple optics suffices. Nearby optical astronomers could provide additional data on seeing.

10 Telescope protection

Presently, many IACTs operate in the open field, without any significant protection during daytime or moon nights, when no data can be taken. The example of the Whipple telescope shows indeed that under certain circumstances a telescope of this size can be operated without further protection. However, while CT cameras can be made reasonably resistant to environmental influences such as dust, mist, rain, snow, or ice, the mirror quality deteriorates noticeably, and mirrors have to be refurbished every few years. Depending on the site, one may in addition encounter massive snow fall, ice, or storms (the Calar Alto, e.g., reports winds with speeds approaching 200 km/h). Under these conditions, the lifetime, efficiency and reliability of the system can be much improved if telescopes can be sheltered while they are not in use. Cost arguments exclude conventional telescope domes. Among the options studied are low cost movable shelters and telescopes which can be moved on rails into storage halls; one hall accepts all telescopes in one row of the array (Fig. 44).

11 Cost Estimates and Funding Profile

11.1 Cost estimates

Given the large number of design options presently under study, it makes little sense to quote detailed cost numbers at this time, although at least for one variant - the Vertex dish combined with aluminum mirrors, and a 271-pixel camera with flash-ADC readout - costs are fairly well known, based on a combination of quotes from potential manufactures for all major parts, and the experience in the construction of the HEGRA IACT cameras. Based on these numbers, we use 1.5 MDM as our present best guess for the cost of a system telescope, excluding site costs and current R&D. Very roughly, costs are equally shared between the telescope mechanics (mount, dish, camera support, and drives), the mirrors (including the cluster mechanics), and the camera with its associated electronics.

11.2 Funding Profile

Based on the preliminary schedule given in the following section, an optimal funding profile for the construction and installation of the first 4-telescope cell would require about 5% of the total funds in 1997, 35% in 1998, 45% in 1999, and 15% in 2000. With relatively minor rearrangements, and without significantly compromising

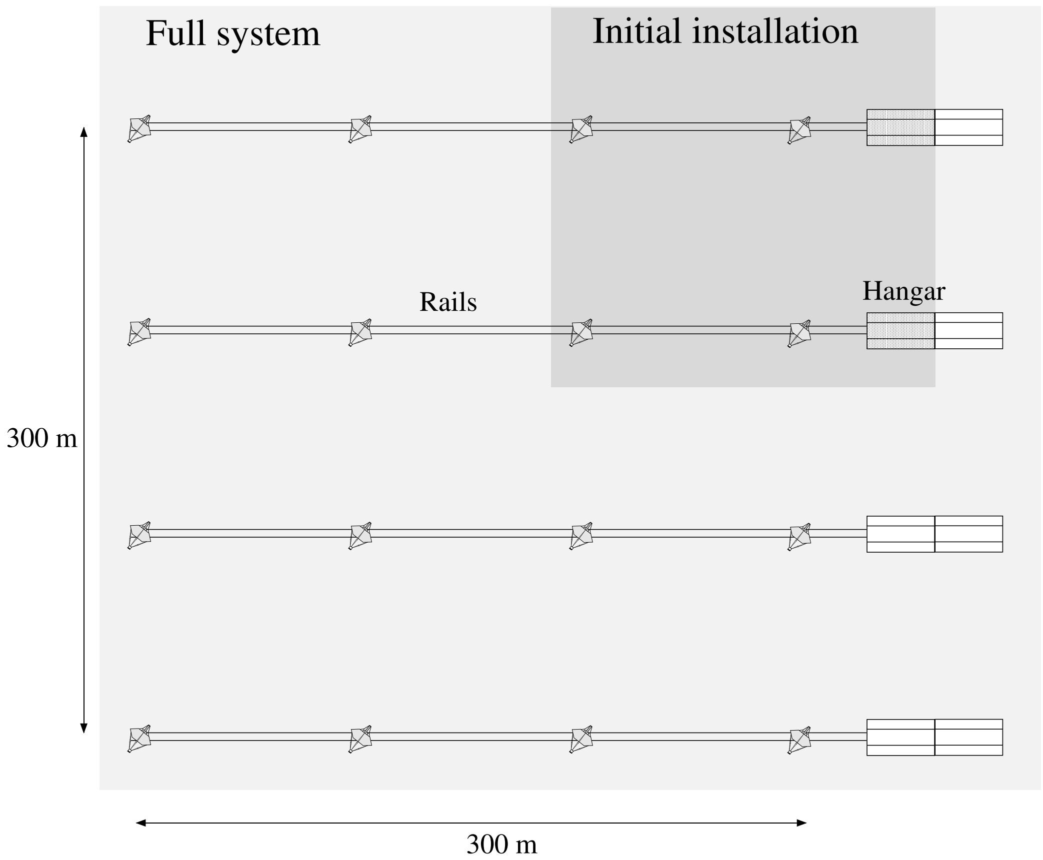

Figure 44: *Scenario with telescopes on rails; during moon periods or bad weather condition, the telescopes are moved into storage hangars. Initially, two rails and two hangars are required; for a larger system, these existing rails and hangars are expanded, and more are added.*

the readiness of the first cell, one might achieve a more realistic profile such as 10% in 1997, and 30% each in 1998, 1999, and 2000.

12 Schedule

Fig. 45 shows a preliminary schedule for the first stage of the project - the first 4-telescope cell. At this stage, with many major hardware decisions still open, such a schedule is obviously rather tentative. The schedule shown represents an optimistic scenario, not limited by funding constraints. The schedule assumes the readout with an ASIC; if the existing FADC-system is used, the electronics part of the schedule is much relaxed. Generally, the year 1997 is required for detailed evaluations of components and manufacturers; all major decisions have to be taken early 1998. Following are two years where components are manufactured, tested, and assembled. Mounts and dishes for all four telescopes are manufactured in parallel. We would aim to install the first telescope in the fall of 1999, and the other three in the spring and early summer of 2000. The winter 1999/2000 could be used for last modifications, based on the experience from the first telescope. To our present knowledge, critical path items include the development of the readout ASIC - a decision to use the small pixel size should only be taken after a first version of the chip is tested - and the mass production of the PMTs (for small pixels) and of the mirrors. The industrial design and production of the mounts and dishes appears relatively uncritical.

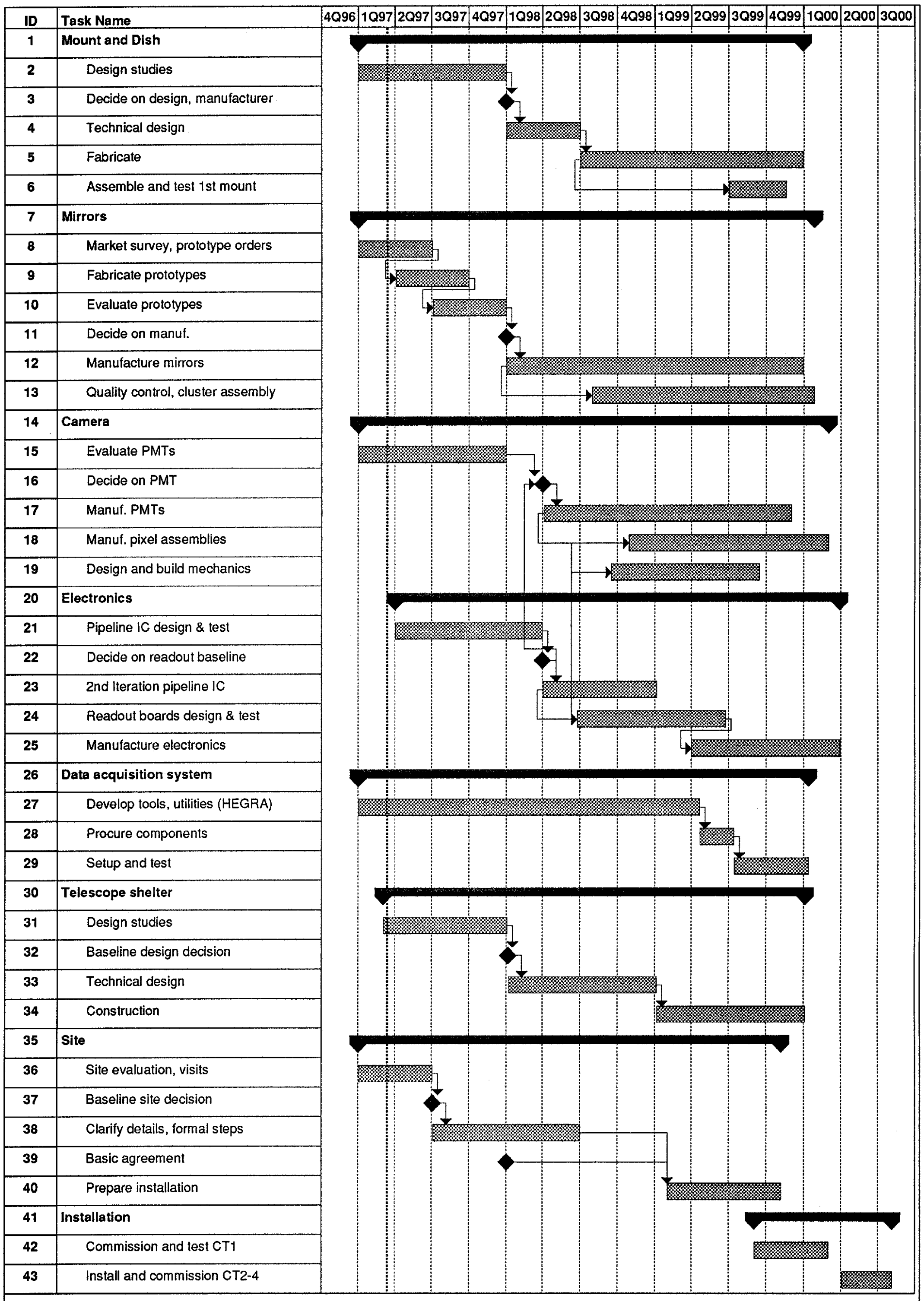

Figure 45: *Preliminary schedule for the first stage of the CT array project.*

References

[1] F. Aharonian, Proceedings of the Int. Workshop "Towards a Major Atmospheric Cherenkov Detector II", Calgary, (1993), R.C. Lamb (Ed.), p. 81.

[2] G. Hermann, Ph.D. Thesis, Heidelberg, 1996, and G. Hermann, Proceedings of the Int. Workshop "Towards a Major Atmospheric Cherenkov Detector IV", Padua, (1995) M. Cresti (Ed.), p. 396.

[3] Max Planck Institut für Kernphysik, Annual Reports 1994,1995.

[4] W. Schönbach, "Stahlbauhandbuch", Ch. 38, Dt. Stahlbau-Verband, Köln.

[5] M. Becker, W. Gupta (Eds.), W. Meinecke, M. Bohn, "Solar Energy Concentrating Systems", C.F. Müller Verlag, Heidelberg, 1995.

[6] W.B. Stine, R.B. Diver (Eds.) "A Compendium of Solar Dish/Stirling Technology", SAND93-7026 UC-236 (1994).

[7] T.A. Sebring et al., Proceedings of the Conf. on "Advanced Technology Optical Telescopes V", Kona, Hawaii (1994), L.M. Stepp (Ed.), SPIE Vol. 2199, p. 565; S.J. Medwadowski, ibid., p. 366; F.B. Ray, ibid, p. 928.

[8] J.M. Davies, E.S. Cotton, J. Solar Energy Sci. and Eng., 1 (1957) 16

[9] "Radio Schmidt Telescope, Phase I, Technical Report", Special Projects Group, Coast Steel Fabricators Ltd., Port Coquitlam, B.C., 1990.

[10] M. Ulrich, Ph.D. Thesis, Heidelberg, 1996, and M. Ulrich, Proceedings of the Int. Workshop "Towards a Major Atmospheric Cherenkov Detector IV", Padua, (1995), M. Cresti (Ed.), p. 121.

[11] D.A. Lewis, Exp. Astronomy 1 (1990) 213.

[12] "The Optical Layout of the HEGRA Cherenkov Telescopes", A. Akhperjanian et al., MPI-H-V46-1995 (1995), to be published.

[13] R. Mirzoyan, Proceedings of the Int. Workshop "Towards a Major Atmospheric Cherenkov Detector IV", Padua, (1995), M. Cresti (Ed.), p. 305.

[14] "Cherenkov Array at Themis" CAT Project Report, B. Degrange et al., (1993), and
M. Punch, Proceedings of the Int. Workshop Towards a Major Atmospheric Cherenkov Detector IV, Padua, (1995), M. Cresti (Ed.), p. 356.

[15] P. Beckmann, in "Progress in Optics", Vol. VI, p. 55, E. Wolf (Ed.), North-Holland (1967).

[16] T. Keck, W. Schiel, A. Schweitzer, Proc. of the 6th Int. Symp. on Solar Thermal Concentrating Technologies, Mojacar, Spain (1992), p. 85; S. Cordes, M. Böhmer, R. Monterreal, idid, p. 97. R. Romero, J.M. Figarola, R. Monterreal, ibid, p. 105.

[17] M. Schenk, "Werkstoff Aluminum und seine Anodische Oxydation", A. Franke AG. Verlag, Bern, 1948.

[18] Th. Fend et al., "Optical Properties and Exposure Tests of Solar Reflective Materials", Proc. of the Eurosun '96 Conf., Freiburg (1996), in print.

[19] G. Jorgensen et al., "International Collaborative Testing of Solar Reflectors", 8th Int. Symposium on Solar Thermal Concentrating Technologies, Köln (1996), in print.

[20] M. Sanchez, M. Romero, Proc. of the 6th Int. Symp. on Solar Thermal Concentrating Technologies, Mojacar, Spain (1992), p. 119.

[21] R. Mirzoyan et al., Nucl. Instr. Meth. A351 (1994) 513.

[22] K. Harris et al., Proceedings of the Int. Workshop "Towards a Major Atmospheric Cherenkov Detector", Palaiseau, (1992), P. Fleury and G. Vacanti (Ed.), p. 189.

[23] F. Aharonian et al., J. Phys. G 21 (1995) 985

[24] "Triggering of Imaging Air Cherenkov Telescopes: PMT Trigger Rates due to Night-Sky Photons", G. Hermann et al., MPI H-V36-1995 (1995).

[25] R. Mirzoyan, Proceedings of the Int. Workshop Towards a Major Atmospheric Cherenkov Detector IV, Padua, (1995), M. Cresti (Ed.), p. 209.

[26] W. Stamm, K. Sauerland, N. Müller, Nucl. Instr. Meth. A328 (1993) 601.

[27] E. Badura, A.H. Walenta, "A 5000-Channel Drift Chamber Read Out System for Collider Experiments", Si 20-9-93 (1993).

[28] R. Brenner et al., Nucl. Instr. Meth. A339 (1994) 564

[29] M. French et al., Proc. First Workshop on Electronics for LHC Experiments, (1995), p. 120.

[30] K.L. Lee et al., "Analog-to-Digital Conversion Using Custom CMOS Analog Memory for the EOS Time Projection Chamber", LBL-29065 (1990).

[31] D. Goldner, R. Horisberger, H. Kolanoski "Study of Time and Charge Resolution of Drift Chamber Pulses Using a Fast VLSI Waveform Sampler Chip", PSI-PR-95-10 (1995).

[32] W. Fallot-Burghardt et al., Proc. of the "Second Workshop on Electronics for LHC Experiments", Balatonfüred (1996).

[33] C. Köhler, Diploma Thesis, Heidelberg 1995; C. Köhler et al., "Trigger Conditions and Effective Areas of Imaging Air Cherenkov Telescopes", MPI H-V17-1996 (1996), and Astroparticle Phys., in print.

[34] J.H. Buckley, Proceedings of the Int. Workshop Towards a Major Atmospheric Cherenkov Detector III, Tokyo, (1994), T. Kifune (Ed.), p. 221.

[35] C.L. Bhat et al., Nucl. Instr. Meth. A 340 (1994) 413.

[36] R. Mirzoyan et al., Nucl. Instr. Meth. A351 (1994) 513.

[37] G. Pühlhofer, Diploma Thesis, Heidelberg 1996.

[38] G. Vacanti et al., Astroparticle Phys. 2 (1994) 1.

[39] J. Rose, Proceedings of the "Int. Workshop Towards a Major Atmospheric Cherenkov Detector IV", Padua, (1995), M. Cresti (Ed.), p. 241.

[40] A. Konopelko et al., Astroparticle Phys. 4 (1996) 199.

[41] W. Stamm, private comm.

[42] C. Wieland, Diploma Thesis, Heidelberg, 1995.